

Molecular gas in low-metallicity starburst galaxies: Scaling relations and the CO-to-H₂ conversion factor[★]

R. Amorín¹, C. Muñoz-Tuñón^{2,3}, J.A.L. Aguerri^{2,3}, and P. Planesas⁴

¹ INAF – Osservatorio Astronomico di Roma, Via Frascati 33, I-00040 Monte Porzio Catone, Roma, Italy

² Instituto de Astrofísica de Canarias (IAC), Vía Láctea S/N, E-38200 La Laguna, Tenerife, Spain

³ Departamento de Astrofísica, Universidad de La Laguna, E-38206 La Laguna, Tenerife, Spain

⁴ Observatorio Astronómico Nacional (IGN), Alfonso XII 3, E-28014 Madrid, Spain

Received ..., ...; accepted ..., ...

ABSTRACT

Context. Tracing the molecular gas-phase in low-mass star-forming galaxies becomes extremely challenging due to significant UV photo-dissociation of CO molecules in their low-dust, low-metallicity ISM environments.

Aims. We aim at studying the molecular content and the star formation efficiency of a representative sample of 21 Blue Compact Dwarf galaxies (BCDs) previously characterized on the basis of their spectrophotometric properties.

Methods. We present CO (1-0) and (2-1) observations conducted at the IRAM-30m telescope. These data are further supplemented with additional CO measurements and multiwavelength ancillary data from the literature. We explore correlations between the derived CO luminosities and several galaxy-average properties.

Results. We detect CO emission in 7 out of 10 BCDs observed. For two galaxies these are the first CO detections reported so far. We find the molecular content traced by CO to be correlated with the stellar and H I masses, star formation rate (SFR) tracers, the projected size of the starburst and its gas-phase metallicity. BCDs appear to be systematically offset from the Schmidt-Kennicutt (SK) law, showing lower average gas surface densities for a given Σ_{SFR} , and therefore showing extremely low ($\lesssim 0.1$ Gyr) H₂ and H₂+H I depletion timescales. The departure from the SK law is smaller when considering H₂+H I rather than H₂ only, and is larger for BCDs with lower metallicity and higher specific SFR. Thus, the molecular fraction ($\Sigma_{\text{H}_2}/\Sigma_{\text{H I}}$) and CO depletion timescale ($\Sigma_{\text{H}_2}/\Sigma_{\text{SFR}}$) of BCDs is found to be strongly correlated with metallicity. Using this and assuming that the empirical correlation found between the specific SFR and galaxy-averaged H₂ depletion timescale of more metal-rich galaxies extends to lower masses, we derive a metallicity-dependent CO-to-H₂ conversion factor $\alpha_{\text{CO,Z}} \propto (Z/Z_{\odot})^{-\gamma}$, with $\gamma = 1.5(\pm 0.3)$ in qualitative agreement with previous determinations, dust-based measurements, and recent model predictions. Consequently, our results suggest that in vigorously star-forming dwarfs the fraction of H₂ traced by CO decreases by a factor of about 40 from $Z \sim Z_{\odot}$ to $Z \sim 0.1Z_{\odot}$, leading to a strong underestimation of the H₂ mass in metal-poor systems when a Galactic $\alpha_{\text{CO,MW}}$ is considered. Adopting our metallicity-dependent conversion factor $\alpha_{\text{CO,Z}}$ we find that departures from the SK law are partially resolved.

Conclusions. Our results suggest that starbursting dwarfs have shorter depletion gas timescales and lower molecular fractions compared to normal late-type disc galaxies even accounting for the molecular gas not traced by CO emission in metal-poor environments, raising additional constraints to model predictions.

Key words. galaxies: evolution – galaxies: general – galaxies: ISM – radio lines: ISM – starbursts

1. Introduction

Blue Compact Galaxies (BCDs) are low luminosity gas-rich systems with an optical extent of a few kpc (Thuan & Martin, 1981). They undergo intense bursts of star formation, as evidenced by their blue colours and strong nebular emission, with ongoing star formation rates (SFR) typically $\sim 0.1 - 10 M_{\odot} \text{yr}^{-1}$ (e.g., Gil de Paz et al., 2003). BCDs span in a wide range of sub-solar metallicities $0.02 \lesssim Z/Z_{\odot} \lesssim 0.5$, including the most metal-poor star-forming galaxies known in the local Universe (e.g., Terlevich et al., 1991; Kunth & Östlin, 2000; Kniazev et al., 2004; Izotov et al., 2006; Papaderos et al., 2006, 2008; Morales-Luis et al., 2011; Filho et al., 2013). These extreme properties lead originally to conjecture that

they are pristine galaxies experiencing at present the formation of their first stellar population (Sargent & Searle, 1970). Subsequent work has shown, however, that most (>95%) BCDs are old systems (> 5 Gyr) that underwent previous starburst episodes (Gerola et al., 1980; Davies & Phillipps, 1988; Sánchez Almeida et al., 2008). This conclusion relies mostly upon the detection of a more extended, evolved low-surface brightness host galaxy (Papaderos et al., 1996a,b; Cairós et al., 2001a; Cairós et al., 2003; Noeske et al., 2003, 2005; Caon et al., 2005; Gil de Paz & Madore, 2005; Vaduvescu et al., 2006; Hunter & Elmegreen, 2006; Amorín et al., 2007, 2009; Micheva et al., 2013). Nonetheless, even though they are not pristine galaxies, nearby BCDs constitute ideal laboratories to study in great detail vigorous star formation and galaxy evolution under physical conditions that are comparable to those present in low-mass galaxies at higher redshift (e.g., Amorín et al., 2015, 2014a,b; Maseda et al., 2014; de Barros et al., 2015).

Send offprint requests to: R. Amorín e-mail: ricardo.amorin@oa-roma.inaf.it

[★] Based on observations carried out with the IRAM 30m Telescope. IRAM is supported by INSU/CNRS (France), MPG (Germany) and IGN (Spain).

So far, our understanding of the main processes triggering and regulating star formation activity in BCDs remains very limited. This is largely due to our poor knowledge of the physical mechanisms behind starburst activity, as well as of the feedback induced by the massive star formation in the interstellar medium (ISM). The strong UV radiation and the mechanical energy from stellar winds and SNe are likely agents of feedback in starbursts like those present in BCDs, leading to the ejection of metal-enriched gas into the galactic halo, limiting the star formation and shaping the large-scale structure and kinematics of the surrounding ISM (e.g., Mac Low & Ferrara, 1999; Silich & Tenorio-Tagle, 2001; Tenorio-Tagle et al., 2006; Recchi & Hensler, 2013).

Likewise, the triggering of the starburst in BCDs remains a puzzle: these low-mass, gas-rich galaxies generally lack density waves and only a small fraction of them are seen in strong tidal interactions or merging with more massive companions (e.g., Campos-Aguilar et al., 1993; Telles & Terlevich, 1995; Pustilnik et al., 2001; Koulouridis et al., 2013). The origin of their ongoing star formation activity has been predominantly associated with fainter interactions with low-mass companions (e.g., Noeske et al., 2001; Brosch et al., 2004; Bekki, 2008), cold-gas accretion (e.g., Sánchez Almeida et al., 2014, 2015) and other, barely understood internal processes (e.g., Papaderos et al., 1996b; van Zee et al., 2001; Hunter & Elmegreen, 2004).

Results from detailed surface photometry have shown that starbursting dwarfs are more compact, i.e., they have a higher stellar concentration, than more quiescent dwarf irregulars (dIs; e.g., Papaderos et al., 1996b; Gil de Paz & Madore, 2005; Amorín et al., 2009). Moreover, spatially resolved H I studies (van Zee et al., 1998, 2001; Ekta & Chengalur, 2010; López-Sánchez et al., 2012; Lelli et al., 2014a,b) have shown both that the central gas surface density in BCDs can be a factor ≥ 2 higher and that their H I gas kinematics is more disturbed than in dIs. Some of these studies suggest that inflows of gas onto a BCD might lead to a critical gas density and, in turn, to the ignition of star formation on a small (~ 1 kpc) spatial scale. In addition, it has been suggested that gravity-driven motions and torques induced by the formation and further interaction of large star-forming clumps may also lead to central gas accretion and angular momentum loss, feeding the current starburst (Elmegreen et al., 2012). Additional observational support to this picture has been recently provided by studies of chemical abundances and ionized gas kinematics in metal-poor starbursts (e.g., Amorín et al., 2010b, 2012; Zhao et al., 2013; Sánchez Almeida et al., 2013, 2014).

A complete understanding of the above scenarios must take into account the relation between the total gas content and the ongoing SFR. In a classical paper Schmidt (1959) suggested the existence of a power-law relation between gas and SFR volume densities in the Milky Way. Later, this relation was calibrated in terms of surface densities by Kennicutt (1998) for a large number of galaxies, including late-type disks and massive starburst galaxies. The tight correlation found between the disk-averaged SFR and the gas (atomic, molecular or the sum of both) surface density, is a power law usually referred to as the “Schmidt-Kennicutt law” (hereafter SK law) and is of the type $\Sigma_{\text{SFR}} \propto \Sigma_{\text{gas}}^N$, with an exponent N typically ranging 1.3–1.5 (e.g., Bigiel et al., 2008; Kennicutt & Evans, 2012). Defining the star formation efficiency (SFE) as the formation rate of massive stars per unit of gas mass able to form stars, or $\text{SFE} \equiv \Sigma_{\text{SFR}}/\Sigma_{\text{gas}}$, the above power law implies that galaxies with higher gas surface density will be more efficient converting gas into stars.

Recent studies have identified the cold molecular gas density to be the primary responsible for the observed star formation rates in star-forming dwarf galaxies (e.g., Bigiel et al., 2008; Schruba et al., 2011). This is in agreement with the fact that massive star clusters occur in giant molecular clouds. The accumulation of large amounts of cold molecular gas would therefore be a prerequisite for the ignition of a starburst, leading to assume that galaxies with vigorous star formation must contain large amounts of H_2 . The knowledge of the H_2 mass, spatial distribution and physical conditions is therefore essential for understanding the star formation processes itself, its ISM chemistry and the galaxy evolution as a whole. In spite of their relevance and the extensive observational effort conducted over the last decade (see e.g., Leroy et al., 2005, 2011; Bigiel et al., 2008; Bolatto et al., 2011; Schruba et al., 2012; Boselli et al., 2014; Cormier et al., 2014), these remain key open questions for star-forming dwarf galaxies.

Due to the lack of a permanent dipole, H_2 emission arises only from hot or warm gas. For this reason, indirect methods are used to estimate the mass of the *cold* H_2 phase of the ISM. The most widely applied tracer is the CO rotational line emission. However, the cold phase of H_2 , as traced by the ^{12}CO molecule at millimetre wavelengths, seems to be mostly elusive in galaxies with metallicity below $\sim 20\%$ solar (e.g., Elmegreen et al., 2013; Rubio et al., 2015). In particular, BCDs are not only metal-poor but also strongly star-forming, a combination of properties that seems to disfavour high CO detection rates ($\lesssim 25\%$, Israel, 2005; Leroy et al., 2005). This problem becomes particularly severe in the lowest-metallicity BCDs ($Z \lesssim 0.1 Z_{\odot}$) for which only upper limits in CO luminosity exists and for which the CO-to- H_2 conversion factor X_{CO} seems to be extremely uncertain, e.g., in the most metal-poor BCDs I Zw 18 and SBS 0335-052 ($Z \sim 0.02 Z_{\odot}$), where even very deep searches for CO have proved fruitless (Leroy et al., 2007; Hunt et al., 2014).

Low metallicity environments imply lower C and O abundances and low dust-to-gas ratios (Draine et al., 2007). This affects the relative CO to H_2 abundances since dust is the site of H_2 formation and also provides much of the far-UV shielding necessary to prevent CO –that is not strongly self-shielding– from photodissociating (Bolatto et al., 2013). Most recent model predictions point to a CO deficiency in low-metallicity star-forming galaxies as due to a decrease of dust-shielding, which leads to strong photo-dissociation of CO by the intense UV radiation fields generated in the star-forming regions (e.g., Wolfire et al., 2010; Gnedin & Kravtsov, 2010; Glover & Mac Low, 2011). Most of these models predict that, while the H_2 clouds survive – via self-shielding or dust shielding – to extreme, metal-poor ISM conditions, CO molecules are increasingly destroyed and therefore the conversion factor X_{CO} depends strongly on the dust content and metallicity (e.g., Pelupessy & Papadopoulos, 2009; Wolfire et al., 2010; Glover & Mac Low, 2011; Krumholz et al., 2011; Dib, 2011; Narayanan et al., 2012).

In this paper we discuss the CO gas content and its relation with the main galaxy-averaged properties of a large sample of BCDs previously studied in a series of papers (Amorín et al., 2009, and references therein). To this aim, we present a small survey of the lowest rotational transitions of ^{12}CO for a sample of ten BCDs. These new data and additional CO measurements obtained from the literature for another eleven BCDs, are combined with a large multiwavelength ancillary data including metallicities, stellar and H I masses and several SFR tracers. These are used to explore scaling relations between the CO luminosity and star formation in BCDs and, in particular, to study the apparent dependence of the molecular and total ($\text{H I} + \text{H}_2$) gas de-

Table 1. CO observations

Galaxy (1)	Other names (2)	RA (3)	DEC (4)	D (5)	t_{int} (6)	θ_b (7)	S/N (8)
Haro 1	NGC 2415	07 36 56.4	35 14 31.0	52.1	26	5.46	6
Mrk 33	Haro 2	10 32 31.9	54 24 03.5	22.3	52	2.32	6
Mrk 35	Haro 3	10 45 22.4	55 57 37.5	15.6	104	1.62	4
Mrk 36	Haro 4	11 04 58.5	29 08 22.1	10.4	106	1.08	<3
Mrk 297	NGC 6052	16 05 12.9	20 32 32.5	65.1	27	6.84	>10
Mrk 314	NGC 7468	23 02 59.3	16 36 18.9	29.0	106	3.02	<3
Mrk 324	UGCA 439	23 26 32.8	18 16 00.0	22.4	80	2.33	<3
Mrk 401	NGC 2893	09 30 17.0	29 32 24.0	24.1	27	2.50	>10
III Zw 102	NGC 7625	23 20 30.1	17 13 32.0	22.7	27	2.36	>10
III Zw 107	PGC 071605	23 30 09.8	25 32 00.2	78.1	168	8.23	<3

Notes.— Columns: (3) and (4) equatorial coordinates, right ascension and declination ($J2000$), of the central pointing; (5) distance in Mpc; (6) total integration time in minutes; (7) CO ($J = 1 \rightarrow 0$) beam-size (HPBW) in kpc; (8) signal-to-noise ratio of the peak CO ($J = 1 \rightarrow 0$) line.

pletion timescales with metallicity. In this analysis, we are able to derive a tight power-law relation for X_{CO} and metallicity, valid for vigorously star-forming dwarfs over nearly one order of magnitude in metallicity.

We organize this paper as follows. In Section 2 and 3 we describe the sample of galaxies, the CO observations, and the ancillary datasets. In Section 4 we present our results, including the derivation of the CO luminosities, masses and surface densities, and we study different correlations with other galaxy-averaged properties, such as metallicity, sizes and stellar and gas masses. In Section 5 we study the position of the BCDs in the star formation laws, while in Section 6 we discuss these results in terms of the star formation efficiency, specific star formation rate and metallicity. Later, in Section 7, we use these results to derive a metallicity dependent CO-to- H_2 conversion factor and derive total molecular masses. We then revisit different scaling relations which are compared with previous observational studies and discussed in terms of recent models. Finally, in Section 8 we summarize our conclusions. Throughout this paper we adopt $H_0 = 75 \text{ km s}^{-1} \text{ Mpc}^{-1}$, $\Omega_0 = 0.3$, $\Omega_\Lambda = 0.7$, and solar metallicity $12 + \log(\text{O}/\text{H}) = 8.7$ (Allende Prieto et al., 2001).

2. Sample of galaxies and CO observations

The sample of galaxies consists of 21 out of 28 BCDs presented and studied by Cairós et al. (2001a,b), which were characterized later in the basis of their spectrophotometric properties in subsequent works (Cairós et al., 2003; Caon et al., 2005; Cairós et al., 2007; Amorín et al., 2007, 2008, 2009; Amorín, 2010a). As discussed in these previous studies, this sample was originally selected as being representative of the BCD class. Thus, it covers the entire range of morphological types, luminosities, colors, gas content, star formation activity and metallicity properties seen in most BCD samples of the literature.

For the present study, we have conducted CO observations for a subset of 10 BCDs (hereafter referred to as *subsample I*). *Sloan Digital Sky Survey* (SDSS) false-color thumbnails for these galaxies are shown Fig. 1. In Table 1 we summarize the basic observational information for the observed galaxies. For the remaining 11 BCDs in the sample (hereafter referred to as *subsample II*) we have compiled CO measurements from several sources in the literature, as described in Section 3.

The observed BCDs have been selected to favour their CO detectability in one or few pointings. They are small in size (optical diameter $< 2''$), with declinations $\delta > 15^\circ$ and show blue colours and strong $\text{H}\alpha$ emission in their centres, indicative of the presence of intense star formation activity.

The observations of the $^{12}\text{CO } J=1 \rightarrow 0$ [ν 115 GHz] and $J=2 \rightarrow 1$ [ν 230 GHz] rotational transitions were obtained during April 25–28, 2006 at the IRAM 30 m telescope (Pico Veleta, Spain). The IRAM telescope provides beam sizes (HPBW¹) of about $22''$ and $11''$ at 115 GHz and 230 GHz, respectively, which allowed us to measure the CO emission on the sample galaxies over physical sizes between ~ 1 and 8 kpc. In the most compact objects, where the star forming regions are located within the host galaxy effective radius ($r_e \sim 1\text{--}2$ kpc, Amorín et al., 2009), a single central pointing was enough to cover the whole CO emission (see Fig. 1). On the other hand, in more extended BCDs the observed CO emission corresponds only to the most luminous regions of the starbursts, so it may be considered as a lower limit to the total CO emission. For all the observed galaxies our CO observations cover at least $\sim 50\%$ of the projected size of starburst (r_{SB} , see Section 3), while for three objects this fraction, $100 \times \theta_b / 2r_{\text{SB}}$, is $\geq 100\%$.

A wobbler switching mode was used at a frequency of 0.5 Hz with a beam throw up to $240''$ in azimuth. Two independent SIS receivers at each frequency (A100, B100 at 3mm and A230, B230 at 1.3mm) were used to observe both polarizations of the CO $J=1 \rightarrow 0$ and $J=2 \rightarrow 1$ transitions simultaneously. The receivers were tuned in single side band, using only the lower band (LSB), which improves the calibration procedure and avoids contamination by other spectral lines in the image band, especially in observations of the calibration sources. The SIS receivers were connected to two filter-banks with resolutions of 1 MHz and 4 MHz at 115 GHz and 230 GHz, respectively, which yields velocity resolutions, δv , of 2.6 km s^{-1} and 5.2 km s^{-1} , respectively. These backends have 512 channels each, covering a total instantaneous velocity range of 1300 and 2600 km s^{-1} . Pointing and focus were checked before each integration on continuum sources and planets. The pointing accuracy was better than $2.5''$ on average. Calibrations were done using the chopper wheel method, by observing strong radio sources (Orion A, CW

¹ HPBW [arcsec] = $2460/\nu$ [GHz], where ν is the observed frequency

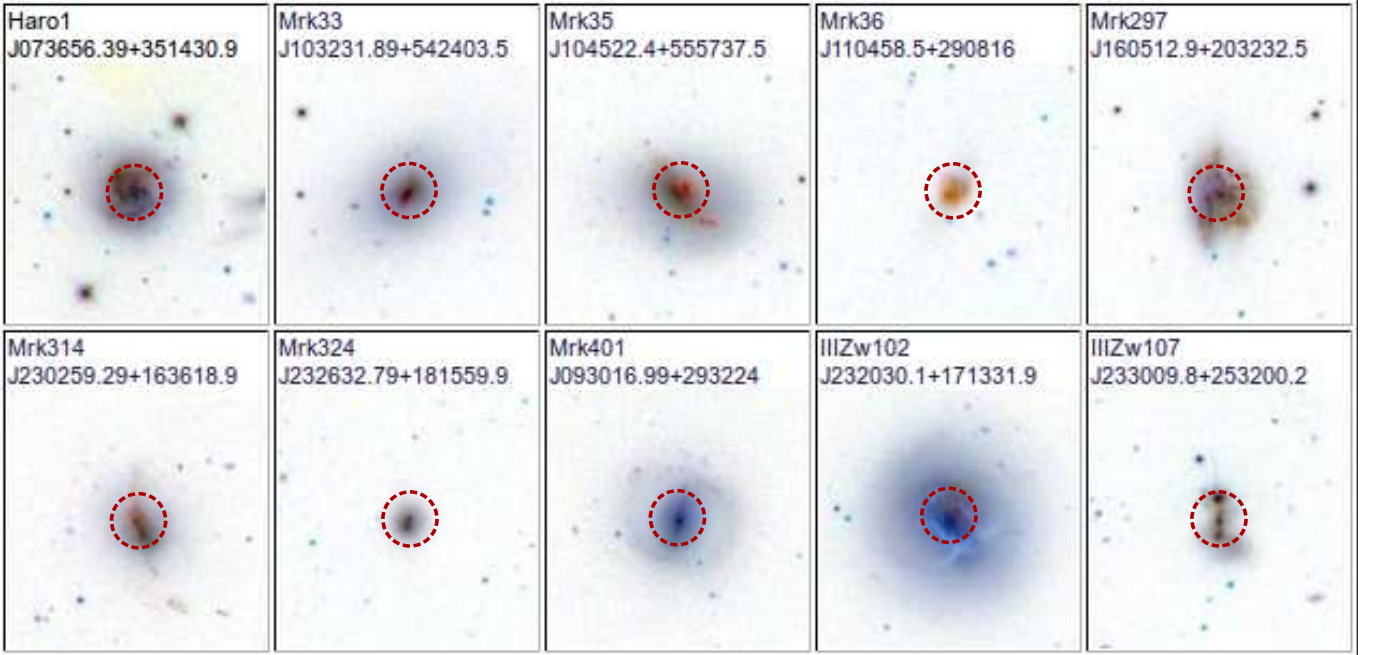


Fig. 1. Inverse *ugriz* color-composite SDSS-DR10 thumbnails of the observed galaxies. Each postage-stamp has $2'$ on a side and a standard NE orientation, while the central circle indicates the center and size of the $22''$ CO ($J = 1 \rightarrow 0$) beam.

Leo, and W51d). System temperatures at both frequencies varied between ~ 290 – 470 K, the higher values due to bad weather conditions. Thus, we obtained a range for the antenna temperature sensitivity of $\delta T_{\text{rms}} \sim 5$ – 15 mK.

The CO spectra was reduced using CLASS² (Buisson et al., 1997). In order to increase the signal-to-noise ratio (S/N) averaged spectra for each pointing was obtained weighting multiple scans by a factor of t/T_{sys}^2 , where t is the integration time and T_{sys} is the system temperature. In all cases, baselines of zeroth order were subtracted. The spectra was then scaled to a main-beam brightness temperature, $T_{\text{mb}} = \frac{F_{\text{eff}}}{B_{\text{eff}}} T_A^*$, where F_{eff} and B_{eff} were the forward and beam efficiencies appropriate to the epoch of observations. These values were 0.95 and 0.75 at 115 GHz, and 0.91 and 0.52 at 230 GHz. Finally, all spectra were smoothed to a resolution $\delta\nu$ of 5 km s^{-1} or 10 km s^{-1} , depending on the S/N.

3. Ancillary datasets

One goal of this paper is to investigate scaling relations between the CO emission and global properties of BCDs (e.g., luminosities, SFRs, metallicities). To this end, we have collected a large multiwavelength dataset from public archives and from the literature, as summarized in Table 2 and Table 3.

We have supplemented our CO observations for *subsample I* with additional measurements for *subsample II* from different studies in the literature. With the aim of getting the more homogeneous dataset as possible, we have compiled the most recent CO ($1 \rightarrow 0$) fluxes, by giving a preference to those derived from observations at the IRAM 30 m telescope, if available.

We have retrieved from the *GALEX* (Martin et al., 2005) archive³ a fully reduced set of far ultra-violet (FUV: $\lambda 1530\text{\AA}$) galaxy images from the All-Sky Imaging Survey (AIS). The an-

gular resolution of the images is about $6''$. Details on the data characteristics can be obtained from Morrissey et al. (2005). After background subtraction we have performed aperture photometry using circular apertures of $22''$, i.e., the same as the CO ($1 \rightarrow 0$) beamsizes. FUV luminosities have been corrected for galactic extinction, using the Schlegel, Finkbeiner, & Davis (1998) dust map and the Cardelli et al. (1989) extinction curve, and for dust attenuation using the prescriptions of Buat et al. (2005), i.e., using the FIR to UV flux ratio.

We use *B*-band absolute magnitudes from (Cairós et al., 2001a). Luminosities and sizes derived for both the BCD host galaxies and their starburst region have been taken from the multi-band 2D surface photometry presented by Amorín et al. (2009). From their study we have also collected stellar masses, which have been derived using the luminosities and colours of the host galaxies and following Bell & de Jong (2001). Typical uncertainties for stellar masses are below a factor of ~ 2 .

In addition, we have collected $H\alpha$ integrated luminosities $L_{H\alpha}$ from Cairós et al. (2001b), Gil de Paz et al. (2003) and López-Sánchez & Esteban (2010), which have been used to derive $H\alpha$ -based SFRs. In the case of UM 462 we have transformed $H\beta$ integral luminosities from Lagos et al. (2007) to $H\alpha$ luminosities using the theoretical Balmer ratio assuming case B recombination with $T_e = 10^4 \text{ K}$ and $n_e = 100 \text{ cm}^{-3}$. For the SFRs, we have used the calibration given by Kennicutt et al. (2009),

$$\text{SFR}(H\alpha) = 7.9 \times 10^{-42} (L_{H\alpha} + 0.0024 L_{\text{TIR}}) [\text{erg s}^{-1}] \quad (1)$$

that accounts for internal dust attenuation using the total infrared (IR) luminosity, L_{TIR} (Dale & Helou, 2002).

The collected IR data consist in *K*-band magnitudes⁴ from the 2MASS extended source catalogue (XSC; Jarrett et al., 2000), and $60\mu\text{m}$ and $100\mu\text{m}$ fluxes (F_{60} y F_{100}) from the *IRAS* Faint Source Catalog (Moshir et al., 1990). The latter were obtained with a beamsizes of $1.44'$ and $2.94'$ respectively, with a

² The CLASS software package is part of the GILDAS software, and can be downloaded from the IRAM website: <http://www.iram.fr/IRAMFR/GILDAS/>

³ <http://galex.stsci.edu/GalexView/>

⁴ In all cases the *K* magnitudes are those obtained with the largest aperture (~ 4 times the *J*-band effective radius).

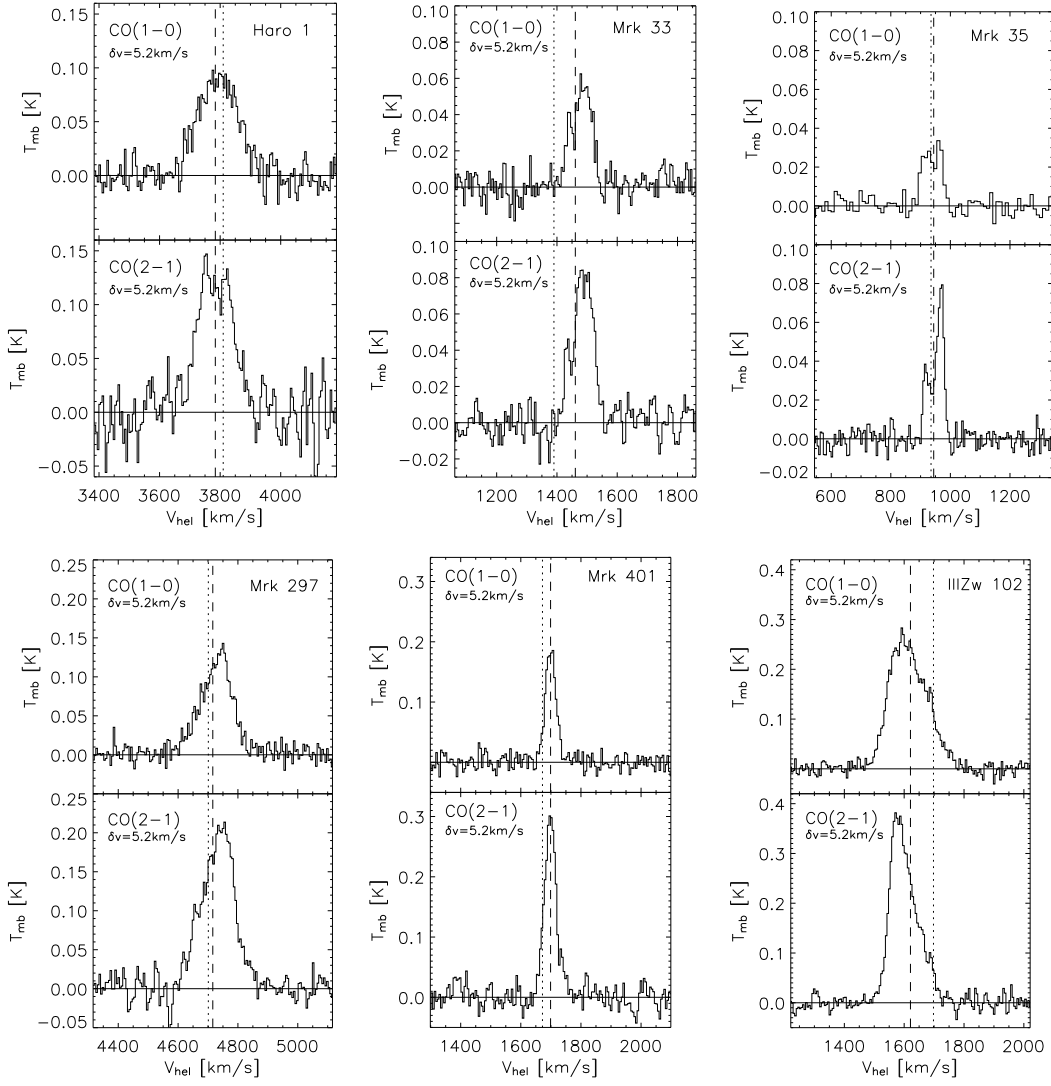


Fig. 2. CO detections: CO $J = 1 \rightarrow 0$ and $J = 2 \rightarrow 1$ spectra are shown for the target galaxies. Horizontal lines indicate the adopted baseline, while vertical lines mark the systemic (heliocentric) velocities as measured from the optical (dotted line) and in 21 cm (dashed lines). The velocity resolution $\delta\nu$, CO transition, and the name of the galaxy are also labelled in each plot.

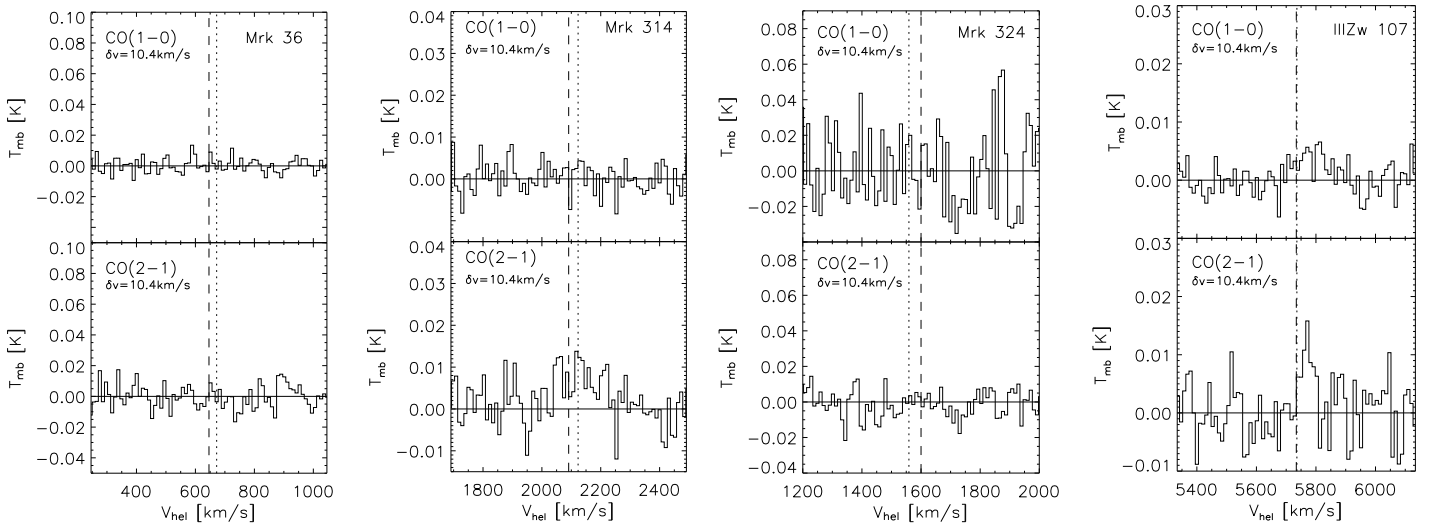


Fig. 3. CO tentative detections and non-detections: symbols, axis and lines are as in Fig 2.

Table 2. Multiwavelength properties of the observed galaxies

Galaxy	r_{25} kpc (2)	r_{SB} kpc (3)	$\sin i$ (4)	M_{HI} $10^9 M_\odot$ (5)	$\log \Sigma_{HI}$ $M_\odot pc^{-2}$ (6)	M_\star $10^9 M_\odot$ (7)	$\log \Sigma_{SFR}$ $M_\odot yr^{-1} kpc^{-2}$ (8)	$12 + \log(O/H)$ dex (9)
Haro 1	6.98	3.33	0.19	6.48	1.32	6.92	-0.52	8.53 ^a
Mrk 33	3.25	1.72	0.72	0.54	0.75	7.41	-1.05	8.35 ^a
Mrk 35	3.07	1.57	0.71	0.68	0.91	2.34	-1.10	8.30 ^{b,c}
Mrk 36	0.45	0.51	0.72	0.03	1.25	0.11	-1.10	7.85 ^a
Mrk 297	8.80	6.31	0.64	11.84	1.28	5.62	-0.41	8.54 ^c
Mrk 314	3.83	1.51	0.82	2.50	1.19	0.38	-1.40	8.11 ^c
Mrk 324	0.82	0.51	0.61	0.23	1.62	0.91	-1.15	8.18 ^e
Mrk 401	3.92	1.69	0.65	0.82	0.81	1.12	-1.30	8.86 ^z
III Zw 102	5.22	2.45	0.24	1.98	1.17	15.85	-0.64	8.74 ^c
III Zw 107	6.82	3.97	0.78	6.69	1.16	2.00	-1.22	8.23 ^d

Columns: (2) radius at the $\mu_B = 25$ mag arcsec⁻² isophote; (3) radius of the star-forming region from 2D surface photometry (Amorín et al., 2009); (4) inclination; (5) H I gas mass; (6) logarithm of H I gas surface density; (7) stellar mass; (8) logarithm of star formation rate density; (9) gas-phase metallicity; references for metallicity: (a) Shi et al. (2006), (b) Cairós et al. (2007), (c) García-Lorenzo et al. (2008), (d) López-Sánchez & Esteban (2010), (e) Zhao et al. (2010), (f) Pérez-Montero & Díaz (2003), (g) Gil de Paz et al. (2003), (h) this work.

Table 3. Multiwavelength properties of galaxies from the literature

Galaxy	r_{25} kpc (2)	r_{SB} kpc (3)	$\sin i$ (4)	M_{HI} $10^9 M_\odot$ (5)	$\log \Sigma_{HI}$ $M_\odot pc^{-2}$ (6)	M_\star $10^9 M_\odot$ (7)	$\log \Sigma_{SFR}$ $M_\odot yr^{-1} kpc^{-2}$ (8)	$12 + \log(O/H)$ dex (9)	$\log \Sigma_{H_2}$ $M_\odot pc^{-2}$ (10)
Haro 15	4.03	3.55	0.78	5.5	1.06	9.92	-1.28	8.33 ^a	<0.62 ^b
Mrk 5	3.04	0.74	0.74	0.14	0.70	0.07	-1.72	8.10 ^a	<0.47 ⁱ
Mrk 86	10.3	1.37	0.49	0.05	0.09	1.75	-1.70	8.53 ^g	0.54 ^k
Mrk 370	7.01	1.01	0.70	0.29	0.74	0.83	-1.66	8.51 ^c	0.44 ⁱ
Mrk 1089	6.04	3.82	0.79	7.46	1.51	3.38	-1.37	8.22 ^d	0.61 ^l
Mrk 1090	2.69	1.66	0.00	1.94	1.33	1.05	-0.92	8.15 ^d	<0.25 ^m
UM 462	3.47	0.92	0.72	0.22	1.15	7.95	-0.80	7.99 ^f	0.22 ^j
I Zw 123	1.39	0.43	0.47	0.06	1.02	0.12	-1.12	7.86 ^a	<0.55 ⁱ
II Zw 40	1.40	0.92	0.79	0.45	1.35	8.09	-0.69	8.07 ^a	0.62 ⁿ
II Zw 70	3.61	1.08	0.97	0.43	0.66	0.10	-1.70	7.69 ^a	<0.27 ^m
II Zw 71	4.05	1.46	0.92	0.95	1.03	0.65	-1.77	8.24 ^a	0.32 ^p

Columns: (2) radius at the $\mu_B = 25$ mag arcsec⁻² isophote; (3) radius of the star-forming region from 2D surface photometry (Amorín et al., 2009); (4) inclination; (5) H I gas mass; (6) logarithm of H I gas surface density; (7) stellar mass; (8) logarithm of star formation rate density; (9) gas-phase metallicity; (10) logarithm of H₂ surface density assuming a Galactic CO-to-H₂ conversion factor; References for metallicity: (a) Shi et al. (2006), (b) Cairós et al. (2007), (c) García-Lorenzo et al. (2008), (d) López-Sánchez & Esteban (2010), (e) Zhao et al. (2010), (f) Pérez-Montero & Díaz (2003), (g) Gil de Paz et al. (2003). References for Σ_{H_2} : (h) Frayer et al. (1998), (i) Leroy et al. (2005), (j) Barone et al. (2000), (k) Albrecht et al. (2004), (l) Leon et al. (1998), (m) Verdes-Montenegro et al. (1998), (n) Taylor et al. (1998), (o) Tacconi & Young (1987), (p) Wei et al. (2010)

pointing error of about 30'' that was used as the search radius around the central target coordinates. Detections have medium or good quality for most of the galaxies, with uncertainties below ~10%, and only for few galaxies, namely Mrk 324, Mrk 36, or III Zw 107 the uncertainties are between 20% and 30%. We calculated FIR and TIR fluxes and luminosities by following the prescriptions of Helou et al. (1988) and Dale & Helou (2002).

Furthermore, we use the H I emission line fluxes, line widths and systemic velocities from Thuan & Martin (1981), and Gordon & Gottesman (1981) (only for Haro 1, Mrk 297 and III Zw 107). The velocity resolution of the data is 13 and 10 km s⁻¹, respectively. We have also used 1.4 GHz continuum luminosities derived from the NRAO VLA Sky Survey (NVSS) (Condon et al., 1998) total fluxes. The spatial resolu-

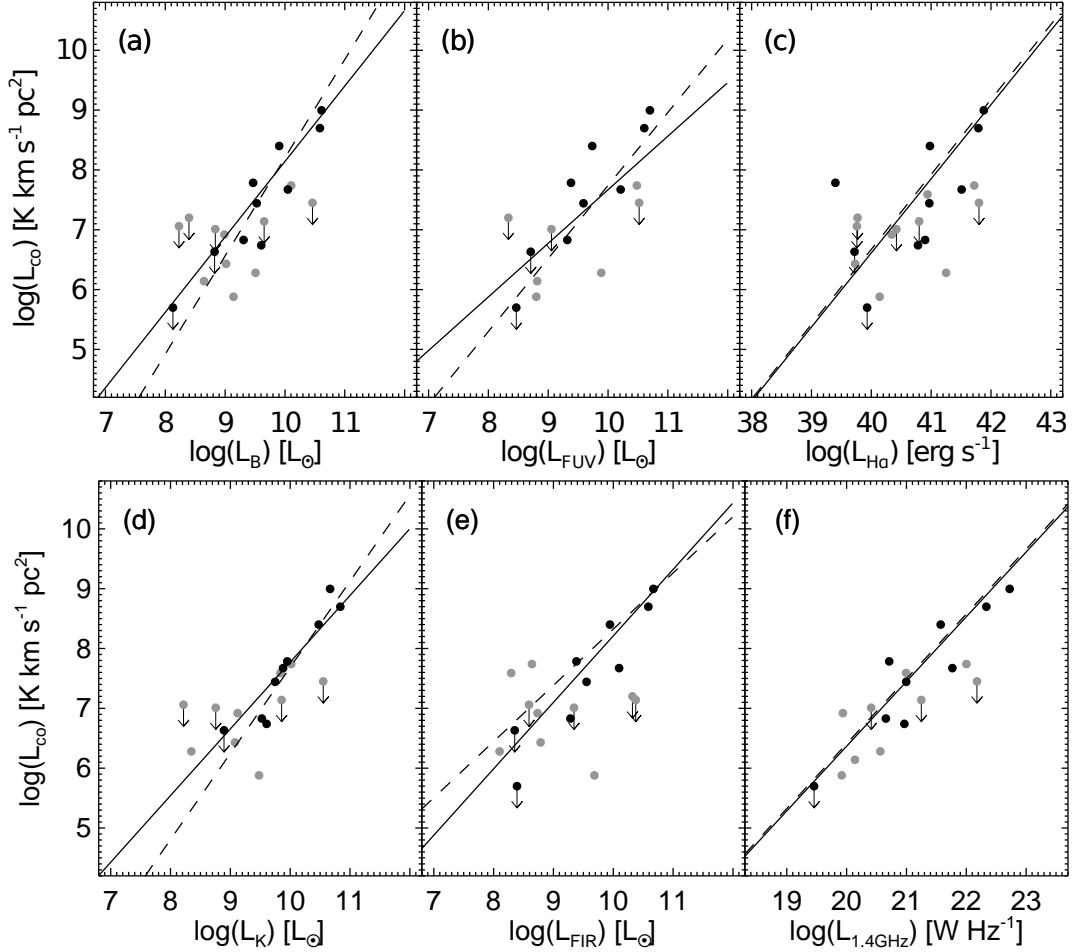


Fig. 4. CO luminosity as a function of luminosity in different wavelength bands: B (a), FUV (b), $H\alpha$ (c), K (d), FIR (e), and 1.4 GHz (f). Black and grey points and lines show *subsample I* and *subsample II* BCDs, respectively. Arrows indicate CO upper limits. Dashed and solid lines indicate linear fits to detected only and all (detected and non-detected) galaxies, respectively.

tion (FWHM) of the NVSS images is $45''$ and the sensitivity limit (rms noise level) is ~ 0.45 mJy beam $^{-1}$.

Finally, we have collected from the literature gas-phase metallicities for the entire BCD sample. They were derived following the direct (T_e) method or strong-line methods calibrated through HII galaxies or Giant HII regions with good determination of the electron temperature, e.g., using the $N2$ ($\equiv \log([NII]/H\alpha)$) index and the relations by Pérez-Montero & Contini (2009). Although this was not possible for the entire sample, for some extended BCDs (e.g., Mrk 35, Mrk 297, Mrk 314, III Zw 102 or Mrk 401) instead of the average (integrated) metallicity, we have used the metallicity measured in the star-forming regions covered by the CO observations. Taken into account the typical uncertainties associated with different metallicity calibrations and methods we have considered an average uncertainty value of ~ 0.2 dex.

4. CO emission in Blue Compact Dwarfs

4.1. Detections and line measurements

In Table 4 we summarize the results from the CO observations, including values for the CO line velocities, line widths, and integrated fluxes. We detect ($\geq 3\sigma$) CO emission in seven out of ten BCDs: Mrk 33, Mrk 35, Mrk 297, Mrk 401, Haro 1, III Zw 102,

and III Zw 107. Two of them, Mrk 401 and III Zw 107, did not presented previous CO detections in the literature⁵. For III Zw 107 we only have 3σ detection at 230 GHz and a marginal detection ($< 3\sigma$) at 115 GHz after smoothing the spectra to 20 km s $^{-1}$. For the three remaining galaxies, Mrk 36, and Mrk 324 are not detected, while Mrk 314 shows a tentative $\sim 2\sigma$ detection only at 230 GHz, with fluxes in good agreement with previous IRAM observations (Garland et al., 2005). The spectra of the galaxies detected in CO are presented in Fig. 2, while spectra of marginally or non-detected galaxies are shown in Fig. 3.

For each detection a Gaussian function was fitted to the CO emission line to determine the central velocity V_{co} , the velocity width at half maximum ΔV_{co} , and the integrated flux $I_{CO} = \int T_{mb} \delta v$. For those BCDs showing more than one velocity component, e.g., Mrk 33 or Mrk 35, we fitted up to two Gaussians. For galaxies showing clear asymmetries in the CO line profile, e.g., Mrk 297 or I Zw 102, we have also estimated I_{co} by the numerical integration of the smoothed spectra within the limits set by the line. In all cases, line flux uncertainties were estimated following Elfhag et al. (1996) and Albrecht et al. (2004). Upper limits for non-detections have been estimated as $I_{co} \lesssim 3\sigma \sqrt{\Delta V_{CO}} \delta v$, where σ is the rms noise level obtained in the baseline range, ΔV_{co} is the expected total velocity width

⁵ Based on the NED: <http://ned.ipac.caltech.edu/>

of the CO line and δv is the channel velocity width. For non-detections we have assumed ΔV_{CO} as the total velocity width of the H α profile. To check the validity of this approximation we have confirmed that, for clearly detected galaxies, the ratio between CO and H α line widths is always below one, regardless of the number of Gaussian components.

4.2. CO luminosity

We derive the CO luminosity of the BCD sample as $L_{\text{CO}} = 23.5 \Omega_{\text{obs}} D_L^2 I_{\text{CO}} (1+z)^{-3}$ [K km s $^{-1}$ pc 2] (Solomon et al., 1997), where I_{CO} refers to the CO (1 \rightarrow 0) integrated fluxes, Ω_{obs} is the observed solid angle at the given frequency and D_L is the luminosity distance of the galaxy. The L_{CO} values for the observed galaxies have been listed in Table 4.

From Fig. 4 to Fig. 8 we investigate scaling relations between L_{CO} and other key properties that are directly connected to star formation activity, as well as stellar and gas content in galaxies. In particular, we use luminosities at different wavelengths such as L_{FUV} , L_{B} , L_{K} , L_{FIR} , $L_{1.4\text{GHz}}$ and $L_{\text{H}\alpha}$, stellar (M_{star}) and total H α gas ($M_{\text{H}\alpha}$) masses, effective radius of the host galaxies (r_e) and projected sizes of the starburst region (r_{SB}), as well as the gas-phase metallicity. Linear least-square fits to data in Figs. 4-8 were performed using the routine FITEXY (Press et al., 1992). The results are presented in Table 5.

In Fig. 4 we show the tight correlation found between the CO luminosity and the luminosities in several wavelength bands, most of them classical tracers of the SFR in galaxies. Overall, we find that less luminous BCDs are also fainter in CO. The fitted relations have slopes between ~ 0.9 -1.5. The derived Spearman rank indices ρ (see Table 5) indicate tight correlations between the luminosities considered. The only exception is L_{FIR} , which shows a large scatter and a lower ρ . The statistical errors provided by the least-square fitting are typically a few %.

In Fig. 5 we also find tentative correlations between the CO luminosity and the total H α gas mass and stellar mass of the BCD hosts. The latter is in relatively good agreement with the L_{CO} - L_{K} relation, as it is expected since the L_{K} is a proxy of stellar mass. Between these two, the relation between L_{CO} and M_{star} show a larger scatter, possibly due to larger uncertainties in the derivation of M_{star} , i.e., in the colours of the host galaxy and given by several assumptions done by models in the derivation of the mass-to-light ratios (e.g., initial mass function or the star formation history, Amorín et al., 2009).

In Fig. 6 we find that the CO luminosity also scales with size. The correlations between both the effective radius of the host galaxy (r_e) and the optical size of their starburst (r_{SB}) indicate that larger BCDs, which have extended and luminous starbursts (Amorín et al., 2009), are best detected in CO than smaller BCDs with more compact star-forming regions.

Finally, in Fig. 7 we show the CO luminosity-metallicity relation. In addition to our galaxy sample we also include in Fig. 7 CO luminosities for several nearby late-type irregular and spiral galaxies from the literature, including upper limits for the most extremely metal-poor BCDs known, I Zw 18 (Vílchez & Iglesias-Páramo, 1998; Leroy et al., 2007) and SBS 0335-052 (Dale et al., 2001; Papaderos et al., 2006). Despite the large scatter, we find a strong positive correlation showing the CO luminosity rapidly increasing with metallicity. The same slope is found if we use I_{CO} instead of L_{CO} , in agreement with previous studies (e.g., Taylor et al., 1998; Schruba et al., 2012).

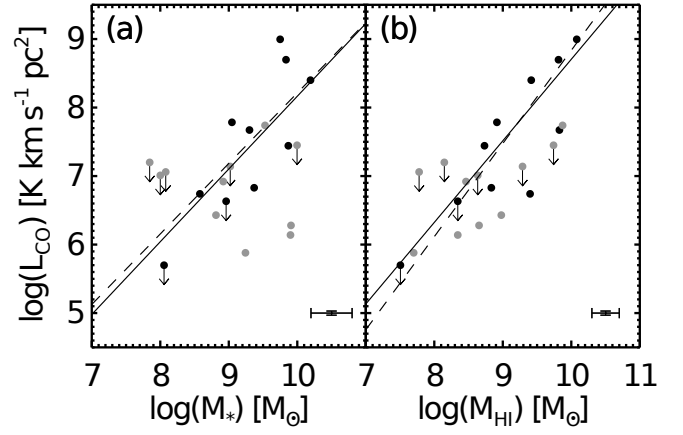


Fig. 5. CO luminosity as a function of stellar mass (a) and H α gas mass (b). Symbols and colours are as in Fig. 4.

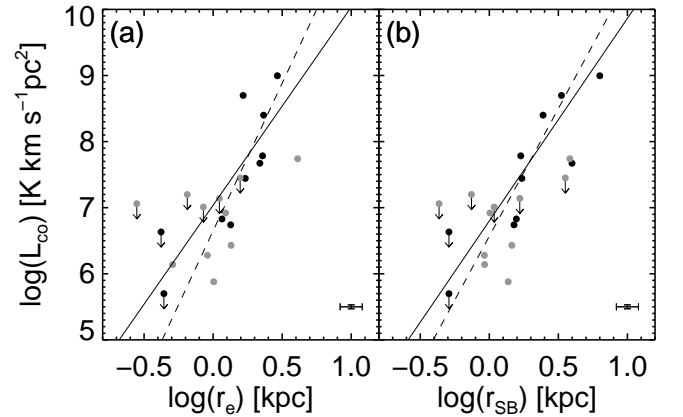


Fig. 6. Relation between CO luminosity and effective radius of the host galaxy (a), and the size of the starburst emission in the optical (b). Symbols and colours are as in Fig. 4.

4.3. Molecular mass and surface densities

The molecular hydrogen mass and surface density traced by CO can be estimated from CO luminosities. Unfortunately, this implies to assume a CO-to-H α conversion factor, X_{CO} , which strongly depends on the physical conditions of the gas (Bolatto et al., 2013, for an extended review). A frequently used X_{CO} value is obtained from Milky Way virialised molecular clouds. For this reason their use in other galaxies must be taken with caution. This is especially true in metal-poor galaxies, since, as we will discuss later, several observational studies have found X_{CO} as a strong function of metallicity (e.g., Rubio et al., 1993; Wilson, 1995; Arimoto et al., 1996; Israel, 1997; Leroy et al., 2011; Genzel et al., 2012; Schruba et al., 2012; Bolatto et al., 2013). Keeping this in mind, we have adopted as a first order approach a constant CO-to-H α conversion factor $X_{\text{CO,MW}} = 2 \times 10^{20}$ cm $^{-2}$ (K km s $^{-1}$) or $\alpha_{\text{CO,MW}} = 3.2 M_{\odot}$ (K km s $^{-1}$ pc 2) $^{-1}$ (Strong & Mattox, 1996; Dame et al., 2001), which is roughly the mean of values estimated in the Milky Way and nearby galaxies. Including a factor of 1.36 due to the contribution of helium, the total molecular mass traced by CO (in solar units) and the CO surface density (in units of M_{\odot} pc $^{-2}$) were then derived as $M_{\text{H}_2} = 1.36 L_{\text{CO}} \alpha_{\text{CO,MW}}$ and $\Sigma_{\text{H}_2} = 1.36 \cos i \alpha_{\text{CO,MW}} I_{\text{CO}}$, where i is the inclination of the galaxies (see Table 2 and Table 3).

Table 4. CO measurements

Galaxy	V_{co} km s ⁻¹	ΔV_{co} km s ⁻¹	$T_{\text{A},1-0}$ mK	$T_{\text{A},2-1}$ mK	$\delta T_{\text{rms},1-0}$ mK	$\delta T_{\text{rms},2-1}$ mK	$I_{\text{co},1-0}$ K km s ⁻¹	$I_{\text{co},2-1}$ K km s ⁻¹	$\log L_{\text{co}}$ K km s ⁻¹ pc ²	$\log \Sigma_{\text{H}_2}$ M _⊙ pc ⁻²
(1)	(2)	(3)	(4)	(5)	(6)	(7)	(8)	(9)	(10)	(11)
Haro 1	3793.0±6	151	73.6	76.0	8.9	12.0	15.1±0.5	19.4±0.8	8.7	1.81
Mrk 33	1482.5±8	85	43.5	46.3	7.0	4.9	4.6±0.3	6.7±0.5	7.4	1.14
Mrk 35	939±6	90	23.6	37.0	5.0	9.2	2.3±0.2	2.0±0.3	6.8	0.85
Mrk 36	646±7	4.7	5.0	<0.4	<0.6	<5.7	<0.10
Mrk 297	4731±5	127	97.7	115	7.2	9.2	19.2±0.6	27.3±0.2	9.0	1.81
Mrk 314	2091±6 ^a	161 ^a	...	5.4	5.6	2.7	<0.6	1.7	6.7 ^a	0.13 ^a
Mrk 324	1600±6	5.6	5.3	<0.7	<0.9	<6.6	<0.39
Mrk 401	1699±6	43	148.6	169.1	6.6	9.1	8.6±0.3	15.2±0.5	7.8	1.46
III Zw 102	1615±4	130	203.7	201.4	15.3	20.7	40.0±0.4	38.3±0.5	8.4	2.23
III Zw 107	5785±11	120	3.7	7.8	2.0	2.6	0.6±0.3	0.7±0.2	7.7 ^a	0.24 ^a

Notes. – Columns: (2) and (3) CO 1→0 line central LSR velocity and width at half maximum; (4)–(5) and (6)–(7) peak intensity and rms of CO 1→0 and CO 2→1 lines, respectively; (8) and (9) integrated line emission and 1σ error bars in T_{mb} units ($I_{\text{co}} = \frac{F_{\text{eff}}}{B_{\text{eff}}} \int T_{\text{A}}^* dv$). 3σ upper limits are given for non-detections; (10) and (11) CO (1→1) luminosity and H₂ surface brightness assuming a Galactic CO-to-H₂ conversion factor. ^a It corresponds to the 2→1 line, which is detected at ~3σ. Its integrated flux was converted to CO 1→0 flux to derive the values in (10) and (11).

Using the above prescriptions, our sample of BCDs show a wide range of CO masses, $M_{\text{H}_2} \sim 2 \times 10^6 - 4 \times 10^9 M_{\odot}$, and CO surface densities, $\Sigma_{\text{H}_2} \sim 1 - 170 M_{\odot} \text{pc}^{-2}$. Most of these values are typical for late-type irregular and spiral galaxies (cf. e.g., Kennicutt, 1998; Leroy et al., 2005), except for the three luminous BCDs of the sample, which are clearly more massive and dense in CO.

5. Star formation laws

In this section we study the relation between star formation rates and gas (molecular and neutral) content averaged over the entire starburst region. In addition to the natural interest of further comparing the results provided by studies on sub-kpc scales, global studies of BCDs can provide an interesting benchmark for future comparison studies with analogues at higher redshifts, for which we can only measure properties at kpc-size scales even using interferometry.

We have explored the position of the BCD sample in the $\Sigma_{\text{SFR}} - \Sigma_{\text{gas}}$ plane and compared with the SK law followed by normal galaxies and luminous starbursts. For that purpose we have derived surface densities in H I (Σ_{HI}), SFR (Σ_{SFR}) and total H I + H₂ gas ($\Sigma_{\text{gas}} = \Sigma_{\text{HI}} + \Sigma_{\text{H}_2}$). We have followed Kennicutt (1998) and adopted a circular aperture for each galaxy that enclose the region where the star-forming regions are distributed. Thus, for the size of each aperture we have used alternatively r_{25} , r_{SB} or the CO beam size after correction for inclination. For the star formation rate we have considered the *ongoing* SFR, as given by the dust-corrected Hα luminosity. The uncertainties for the SFR and gas surface densities are mainly dominated by possible galaxy to galaxy variations in the apertures considered. For the following analysis, we acknowledge a conservative, average uncertainty of ~0.3 dex for surface densities, which do not account by uncertainties in the CO-to-H₂ conversion factor and by assumptions involved in the derivation of SFR (e.g., the tracer and IMF in use or the adopted SF history).

In Figure 8 we present the BCD SFR surface density as a function of their H₂ and H₂ + H I surface densities. In

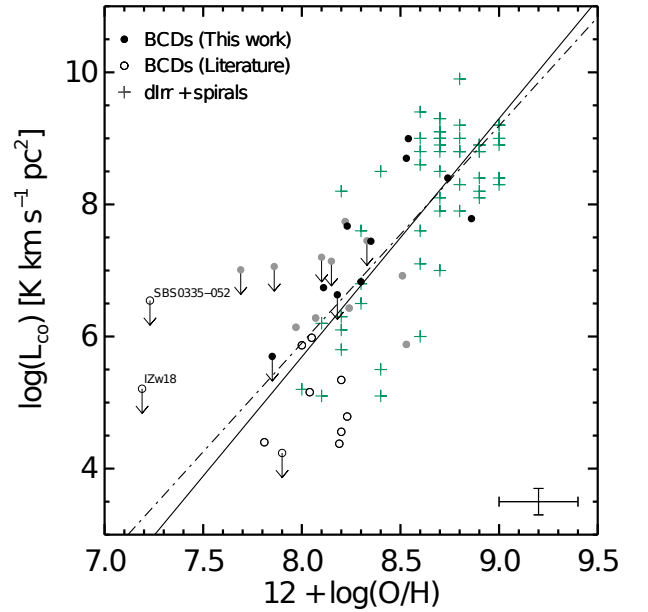


Fig. 7. CO luminosity as a function of metallicity. Black dots show *subsample I* while open circles show *subsample II*, and additional very low-metallicity BCDs compiled from the literature (Fumagalli et al., 2010). Green crosses show the compilation of nearby star forming disc galaxies in Krumholz et al. (2009). Lines indicate linear best-fits to all galaxies (solid) and BCDs only (dashed). Error bars indicate typical uncertainties for our sample.

this figure we have also included the data (spiral discs and starburst galaxies) used by Kennicutt (1998) for the calibration of the SK law. Instead of including the fit by Kennicutt (1998), we have included in Fig. 8a a slightly different fit ($\Sigma_{\text{SFR}} = 10^{-3.4} \Sigma_{\text{H}_2}^{1.3}$) found by Leroy et al. (2005) for a large sample of dwarf irregular galaxies and normal spirals. Similarly, in Fig. 8b we have included the fit presented by Shi et al. (2011)

Table 5. Correlations

x (1)	y (2)	Sample (3)	a (4)	b (5)	ρ (6)
$\log(L_B)$	$\log(L_{CO})$	det	1.64 ± 0.01	-8.20 ± 0.08	0.77
		all	1.26 ± 0.01	-4.46 ± 0.04	0.71
$\log(L_{FUV})$	$\log(L_{CO})$	det	1.22 ± 0.02	-4.46 ± 0.14	0.76
		all	0.89 ± 0.01	-1.28 ± 0.09	0.75
$\log(L_{H\alpha})$	$\log(L_{CO})$	det	1.25 ± 0.01	-43.4 ± 0.36	0.70
		all	1.24 ± 0.01	-42.9 ± 0.20	0.79
$\log(L_K)$	$\log(L_{CO})$	det	1.44 ± 0.01	-6.70 ± 0.07	0.94
		all	1.11 ± 0.01	-3.38 ± 0.05	0.83
$\log(L_{FIR})$	$\log(L_{CO})$	det	0.94 ± 0.01	-1.07 ± 0.07	0.57
		all	1.11 ± 0.01	-2.90 ± 0.05	0.57
$\log(L_{1.4GHz})$	$\log(L_{CO})$	det	1.08 ± 0.01	-15.3 ± 0.1	0.85
		all	1.08 ± 0.01	-15.3 ± 0.1	0.85
$\log(M_*)$	$\log(L_{CO})$	det	1.03 ± 0.01	-2.08 ± 0.06	0.59
		all	1.06 ± 0.01	-2.45 ± 0.04	0.40
$\log(M_{HI})$	$\log(L_{CO})$	det	1.36 ± 0.01	-4.76 ± 0.08	0.77
		all	1.19 ± 0.01	-3.20 ± 0.04	0.72
$\log(r_e)$	$\log(L_{CO})$	det	4.47 ± 0.01	6.65 ± 0.03	0.86
		all	2.99 ± 0.01	7.03 ± 0.01	0.74
$\log(r_{SB})$	$\log(L_{CO})$	det	3.86 ± 0.01	6.57 ± 0.02	0.86
		all	3.06 ± 0.01	6.80 ± 0.01	0.77
$12 + \log(O/H)$	$\log(L_{CO})$	BCD	3.80 ± 0.03	-24.9 ± 0.20	0.76
		all	3.23 ± 0.02	-20.1 ± 0.17	0.77
$12 + \log(O/H)$	$\log(\Sigma_{H_2}/\Sigma_{HI})$	det	2.38 ± 0.32	-20.13 ± 2.74	0.85
		all	1.98 ± 0.23	-16.75 ± 1.88	0.87
$12 + \log(O/H)$	$\log(\Sigma_{H_2}/\Sigma_{H_2+HI})$	det	1.29 ± 0.32	-11.28 ± 2.74	0.87
		all	1.17 ± 0.23	-10.30 ± 1.88	0.85
$12 + \log(O/H)$	$\log(\Sigma_{SFR}/\Sigma_{H_2})$	det	-1.91 ± 0.32	17.00 ± 2.74	-0.92
		all	-1.43 ± 0.23	12.92 ± 1.88	-0.82
$12 + \log(O/H)$	$\log(\Sigma_{SFR}/\Sigma_{H_2+HI})$	det	-0.62 ± 0.32	5.72 ± 2.73	-0.33
		all	-0.26 ± 0.23	2.62 ± 1.88	-0.17

Notes.— Columns (4) and (5) show the best-fit coefficients, slope a and intercept b with their 1σ dispersion, in the relations ($y = ax + b$) between quantities in Cols. (1) and (2). Column (3) indicates the sample of galaxies considered to make the linear fits: galaxies including detections and upper limits (all), and only detected galaxies (det). Column (6) lists the Spearman rank index ρ .

($\Sigma_{SFR} = 10^{-3.9} \Sigma_{H_2+HI}^{1.4}$) for a largest sample of late-type, early-type, and starburst galaxies at low and high redshift, which includes the sample of galaxies studied by Kennicutt (1998). The relation of Shi et al. (2011) is also in excellent agreement with the more recent update of the SK relation by Kennicutt & Evans (2012).

Overall, Fig. 8 shows the BCD sample located in a region corresponding to depletion timescales for both molecular and molecular plus atomic gas of less than 1 Gyr, showing surface densities in smaller than starbursts and larger than spiral and irregulars discs. Remarkably, for most BCDs in our sample the depletion timescales appear to be up to ~ 2 dex lower than expected from the SK-laws. In particular, Fig. 8a shows that most BCDs have lower Σ_{H_2} than the one predicted by the Leroy et al. (2005) relation for a given Σ_{SFR} . Consequently, their H_2 depletion timescales are extremely short (< 0.1 Gyr). Considering the total gas (H_2+HI) surface density, most BCDs still show a systematic departure of up to ~ 1 dex from the SK relation to low

τ_{H_2+HI} that is slightly larger than observational uncertainties, as shown in Fig. 8b.

Large offsets from the SK law for metal-poor star forming galaxies have been reported in previous studies. Rather than galaxies with enhanced SF efficiency or following a distinct SF law, these offsets have been attributed to changes in the CO-to- H_2 conversion factor at low metallicities (e.g., Kennicutt & Evans, 2012). If instead of using a Galactic conversion factor $\alpha_{CO,MW}$ we adopt a metallicity-dependent α_{CO} value (e.g., Arimoto et al., 1996), those BCDs with strongly sub-solar metallicities would be displaced to higher gas surface densities and larger depletion timescales (large arrows in Fig. 8). Additional support to this interpretation comes from the most luminous galaxies of the sample, Mrk 297, III Zw 102, and Haro 1, which are the only BCDs that seem to follow the SK relations. These galaxies show significantly higher gas and SFR densities, placing them at the lower end of the trend followed by the IR-selected starbursts of Kennicutt (1998). Up to some point this

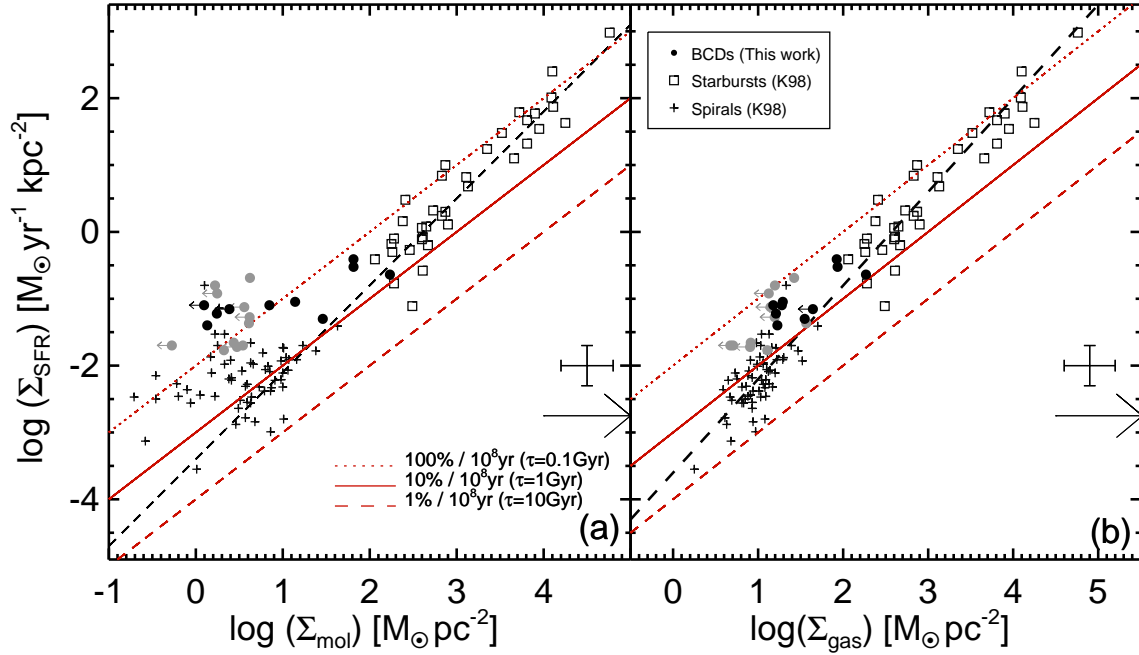


Fig. 8. Star formation rate surface density as a function of H_2 (Left) and H_2+HI (Right) gas surface densities. Black dots show *subsample I* and grey dots show *subsample II*. The black dashed lines show the fits to the H_2 and H_2+HI SK law by Leroy et al. (2005) and Shi et al. (2011), respectively. Red lines indicate constant star formation efficiencies (depletion timescales). Large arrows indicate the shift in H_2 surface density by assuming a CO-to- H_2 conversion factor 10 times larger than that of the Milky Way for the molecular mass. Error bars indicate typical uncertainties for our sample.

is not surprising, since these objects are luminous in IR wavelengths, showing clear dust patches/lanes and complex/distorted morphologies in their inner regions (Cairós et al., 2001a,b, see also our Fig. 1) compatible with past or recent mergers. Perhaps most importantly, these galaxies are the most metal-rich starbursts in the sample.

In the following sections we discuss in detail how metallicity affects the molecular gas depletion timescales in the extreme ISM conditions (i.e., high ionization and high *specific* SFR) of BCDs. This will lead us to find a method for deriving a metallicity-dependent form of α_{CO} that in turn allows us to derive corrected H_2 masses and revise our scaling relations accordingly.

6. Gas depletion timescales and metallicity

In Figure 9 we investigate as a function of metallicity the following quantities: (a) the molecular to atomic surface density ratio (i.e., $R_{H_2} = \Sigma_{H_2}/\Sigma_{HI}$), (b) the molecular to total (H_2+HI) gas surface density ratio (i.e., the molecular fraction $f_{H_2} = \Sigma_{H_2}/\Sigma_{H_2+HI}$) and, (c) and (d) the molecular and total gas (H_2+HI) SFE and their inverse quantity, the gas depletion timescale τ_{H_2} and τ_{H_2+HI} , respectively. The coefficients of the best-fit relations shown in Figure 9 are presented in Table 5.

In Figures 9a–b we show that lower R_{H_2} and f_{H_2} are found for BCDs of increasingly lower metallicities. On the other hand, in Fig. 9c we find a strong anticorrelation, showing a fast decrease of the SFE from low- to high-metallicity BCDs. The latter implies that the H_2 depletion timescale in BCDs is an increasing function of metallicity, showing a large variation in τ_{H_2} (up to a factor of ~ 50), from ~ 0.02 Gyr for BCDs with $Z \sim 0.1 Z_\odot$ to ~ 1 Gyr for BCDs with nearly solar abundance. The relation found between $\Sigma_{SFR}/\Sigma_{H_2}$ and metallicity in Fig. 9c appears in good qualitative agreement with model predictions by Krumholz et al.

(2011, magenta lines, see also Krumholz et al. 2009). Finally, the dependence of the SFE on metallicity is significantly weaker when we consider the total gas surface density, as shown in Fig. 9d.

Short depletion timescales for H_2 in low-mass spirals and nearby dwarf galaxies have been previously reported in the literature (e.g., Leroy et al., 2006, 2007). Although, on average, molecular gas in nearby disk galaxies is consumed uniformly, i.e., the efficiency with which molecular gas forms stars does not depend on the surface density of H_2 averaged over large scales (Bigiel et al., 2008, 2011; Leroy et al., 2008; Schruba et al., 2011), variations in the SFE among galaxies are usually found. Thus, least massive galaxies tend to show shorter depletion timescales for molecular gas than more massive systems (e.g., Gratier et al., 2010a; Schruba et al., 2011; Saintonge et al., 2011; Leroy et al., 2013).

In star-forming dwarf galaxies, where the range of metallicities is large, i.e., from nearly solar to few per cent solar, H_2 depletion timescales are generally lower than ~ 2 Gyr, the galaxy-averaged value found in late-type disks (Bigiel et al., 2008). For example, using dust-based H_2 masses at spatial scales ≥ 1 kpc of the Small Magellanic Cloud Bolatto et al. (2011) found $\tau_{H_2} \sim 0.6$ – 1.6 Gyr. Also, Schruba et al. (2012) found that τ_{H_2} for a sample of 16 nearby ($D \sim 4$ Mpc) star-forming dwarf galaxies from the HERACLES CO survey (Leroy et al., 2008) is one or two orders of magnitude smaller than in normal spiral discs. They concluded that the inferred low values of τ_{H_2} may either indicate low H_2 masses coupled with high SFEs or that CO becomes a poor tracer of H_2 for these galaxies.

In the above studies, however, most nearby dwarfs studied in detail are dwarf Irregulars (dI), while BCDs are strongly underrepresented. Dwarf irregulars form stars at lower rates and their star formation histories are predominantly continuous, i.e., they are main sequence galaxies in the SFR- M_* relation

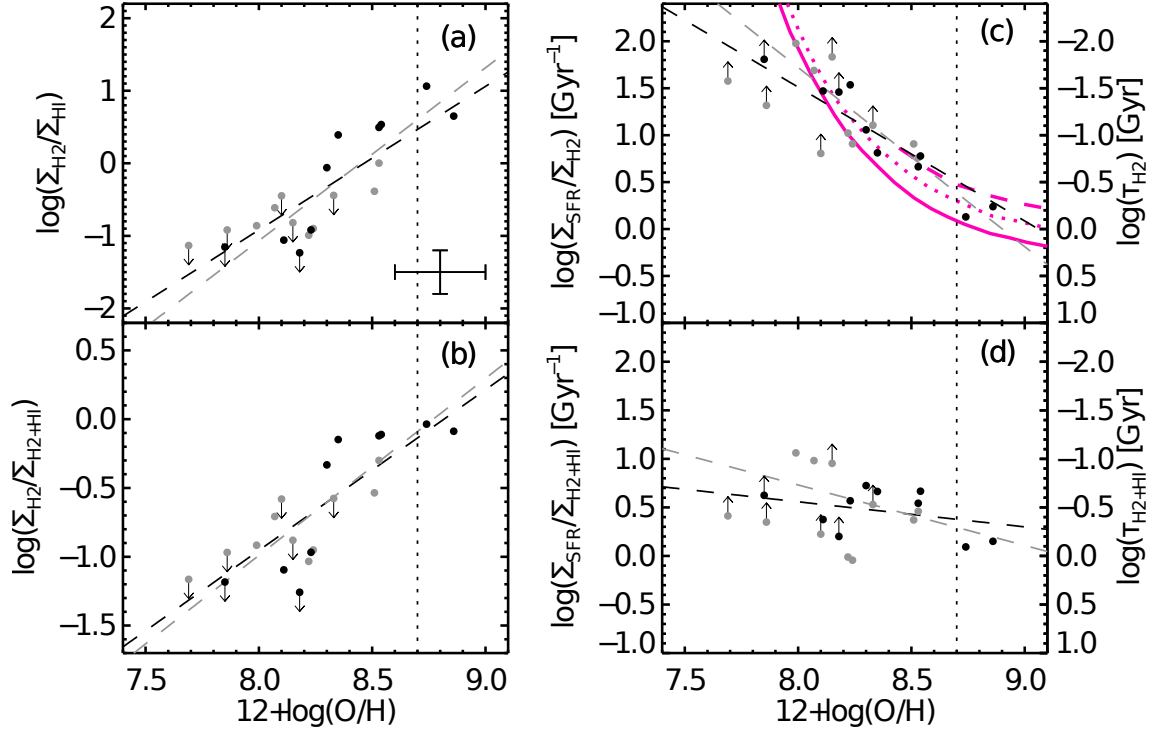


Fig. 9. The molecular to atomic ratio (a), the molecular fraction (b), and the H₂ and H₂+HI depletion timescale (c and d, respectively) as a function of metallicity. Symbols are as in Fig. 8. Black and grey dashed lines show linear best-fits to all data points and only secure detections, respectively. Solid, dotted and dashed magenta lines in panel c show model predictions by Krumholz et al. (2011) for different values of $\Sigma_{\text{H}_2+\text{HI}}$ (80, 20 and 5 $\text{M}_\odot \text{pc}^{-2}$, respectively).

(e.g., Brinchmann et al., 2004; Noeske et al., 2007; Lee et al., 2011; Hunt et al., 2012). In contrast, BCDs show more extreme conditions (e.g., high ISM ionization and higher *specific* SFR (sSFR); Hunt et al., 2012; Amorín et al., 2014a, 2015), thus having predominantly bursty star formation histories (e.g., Martín-Manjón et al., 2012). Therefore, one can argue that part of the enhancement in the SFE of BCDs seen in the SK law is due to a more bursty SF history. In this line, previous studies based on FIR/sub-mm data have found that even using a higher CO-H₂ conversion factor, the depletion timescales for molecular gas in some metal-poor star forming galaxies appear considerably higher than for normal spirals (e.g., Israel, 1997; Gardan et al., 2007; Gratier et al., 2010a,b).

Following the above reasoning in Fig. 10 we investigate the relation between sSFR and both H₂ depletion timescale and metallicity. On average, we find that high sSFR BCDs have lower metallicity (Fig. 10a). These high sSFR galaxies also show higher HI gas mass fractions (red circles). Despite the large scatter, Fig. 10b suggests that BCDs with higher sSFR tend to have shorter τ_{H_2} . A similar trend was presented by Saintonge et al. (2011, dashed line in Fig. 10b)⁶ for more massive ($M_\star \gtrsim 10 \text{ M}_\odot$) star-forming galaxies of the COLDGASS survey (Saintonge et al., 2011). In their sample, however, the sSFR is not correlated with metallicity. In Fig. 10b our BCDs follow the slope of the relation for the COLDGASS sample, but they appear shifted to significantly shorter H₂ depletion timescales for a given sSFR. These results are consistent with Leroy et al. (2013), who found that the eight less massive ($< 10^{10} \text{ M}_\odot$) galaxies in the HERACLES survey are systemati-

cally offset to larger τ_{H_2} for a given sSFR when compared to more massive galaxies.

Taken together, results from Fig. 9 and Fig. 10 are mutually consistent and allow us to conclude that less massive and more metal-poor gas-rich galaxies, which form stars at higher rates, are those with shorter H₂ depletion timescales.

In the next section we use these findings to derive a CO-to-H₂ conversion factor for BCDs, derive their H₂ masses, and revisit the scaling relations between star formation, gas content and metallicity.

7. Deriving a metallicity-dependent CO-to-H₂ conversion factor for starbursting dwarfs

In order to derive an expression for a metallicity-dependent CO-to-H₂ conversion factor we use that $\alpha_{\text{CO,Z}}/\alpha_{\text{CO,MW}} \equiv \tau_{\text{H}_2} \times \Sigma_{\text{SFR}}/\Sigma_{\text{H}_2}$, where τ_{H_2} is the expected galaxy-averaged H₂ depletion timescale for which metallicity effects have been accounted for. Using the relation found between $\Sigma_{\text{SFR}}/\Sigma_{\text{H}_2}$ and metallicity (Table 5), we arrive to the following expression,

$$\log(\alpha_{\text{CO,Z}}/\alpha_{\text{CO,MW}}) = \log(2.4\tau_{\text{H}_2}) - 1.91(12 + \log(\text{O/H}) - 8.7)(2)$$

with a 1σ dispersion of 0.32 in the slope. Possible systematic uncertainties not included in Eq. 2, e.g., those propagated from the derivation of integrated properties and driven by the numerous assumptions made, are likely larger and have not been taken into account.

In order to derive a suitable value for the CO-to-H₂ conversion factor Eq. 2 yet requires the use of an appropriate value for τ_{H_2} . One possibility would be to derive H₂ masses from dust

⁶ The relation given by Saintonge et al. (2011) does not include Helium in Σ_{H_2} , so we have corrected upwards their relation to be consistent with our measurements.

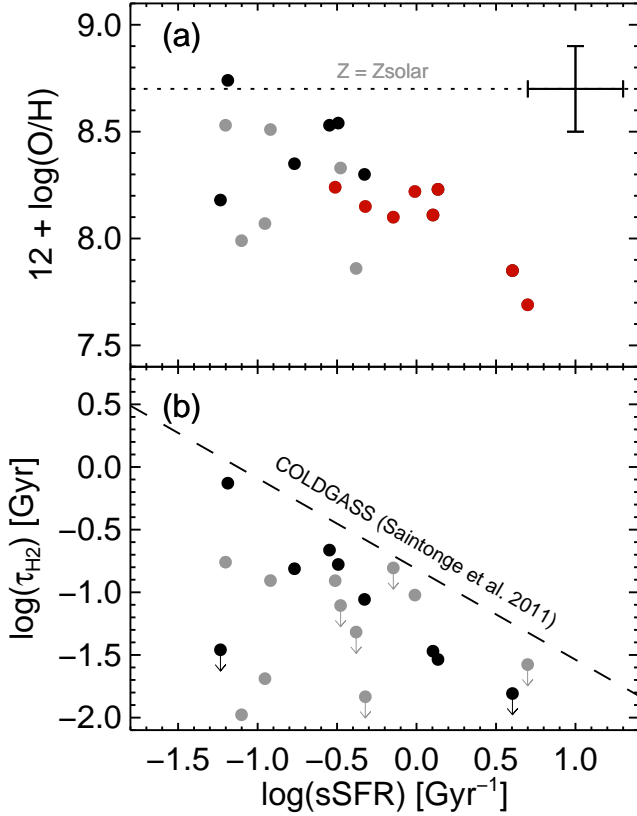


Fig. 10. Metallicity (a) and H_2 depletion timescale (b) as a function of *specific* SFR. Symbols are as in Fig. 9, but red points in a indicate BCDs with higher gas fractions ($M_{\text{HI}}/(M_{\text{HI}} + M_*) > 0.5$) BCDs. The dotted line in a indicates solar metallicity while the dashed line in b shows the correlation found by Saintonge et al. (2011) for local star-forming disk galaxies of stellar masses $M_* \gtrsim 10^{10} M_\odot$.

masses by assuming a dust-to-gas (D/G) ratio, and then compute τ_{H_2} . Especially in compact low-metallicity galaxies this approach is however not free of large uncertainties, which are mostly driven by variations in the D/G ratio with the ISM density (Schruba et al., 2012), uncertainties in its calibration at different metallicities, and variations with the SF history of each galaxy (Cormier et al., 2014; Rémy-Ruyer et al., 2014, see also Bolatto et al. 2013). In our case, only $\sim 20\%$ of the BCD sample have Herschel observations reported so far (see Rémy-Ruyer et al., 2015), thus precluding a complete analysis based on the dust masses.

Another method recently used in the literature relies on the underlying assumption of a constant SFE (τ_{H_2}) for all galaxies (e.g., Schruba et al., 2012; Genzel et al., 2012, see also McQuinn et al. 2012). This method has been motivated by the relatively constant SFE found observations of nearby disk galaxies (Bigiel et al., 2008, 2011; Leroy et al., 2008) and recent theoretical work (e.g., Krumholz et al., 2011) showing that the H_2 gas depletion timescale is uniform and does not depend on metallicity. However, in view of Fig. 10, the hypothesis of a constant τ_{H_2} appear not particularly appropriate for dwarf galaxies with predominately bursty SF histories.

Therefore, in this work we choose an alternative method for obtaining τ_{H_2} for each galaxy assuming that this quantity should follow a well established linear relation with sSFR at all masses (e.g., Saintonge et al., 2011; Boselli et al., 2014;

Huang & Kauffmann, 2014). In particular, here we use the relation derived by Saintonge et al. (2011) for star forming galaxies of stellar masses $M \gtrsim 10^{10} M_\odot$ in the COLDGAS survey (Fig. 10), under the reasonable assumption that it extends to lower stellar masses (dashed line in Fig. 10). Thus, we obtain the expected τ_{H_2} from the ratio between the observed τ_{H_2} computed via the galactic CO-to- H_2 conversion factor and the linear fit of Saintonge et al. (2011) for a given sSFR (Fig. 10 b). Finally, we use this value and Eq. 2 and derive $\alpha_{\text{CO}}(Z)$ for each galaxy.

In Figure 11 we show the derived α_{CO} as a function of metallicity. Despite the large scatter $\log \alpha_{\text{CO}}$ appear to scale linearly with metallicity, meaning that $\alpha_{\text{CO}} \propto (Z/Z_\odot)^{-1.5}$. This relation is in qualitative agreement with previous determinations, dust-based measurements, and recent model predictions, as we discuss below. Fig. 11 suggests that in vigorously star-forming dwarfs the fraction of H_2 traced by CO decreases a factor of about 40 from $Z \sim Z_\odot$ to $Z \sim 0.1Z_\odot$, leading to a strong underestimation of the H_2 mass in metal-poor systems when a Galactic $\alpha_{\text{CO,MW}}$ is considered.

In Figure 11 we have included dust-based α_{CO} measurements for the five BCDs in the sample with Herschel data (red dots). We have used the dust masses compiled by Rémy-Ruyer et al. (2014, 2015) to derive the H_2 masses following Cormier et al. (2014) and assuming the metallicity dependent D/G ratio of Rémy-Ruyer et al. (2015). The resulting dust-based M_{H_2} and $\alpha_{\text{CO,dust}}$ are a factor of ~ 1.5 -30 higher than those derived using the Galactic $\alpha_{\text{CO,MW}}$. Within the errors (larger than a factor of 2), the dust-based measurements are consistent with those based on our method and with the best-fit relation ($\alpha_{\text{CO,Z}} \propto (Z/Z_\odot)^{-1.5}$) shown in Figure 11.

Similarly, our relation is broadly consistent with independent measurements of α_{CO} based on different methods for other nearby star-forming galaxies of sub-solar metallicity. For example, our data are consistent with values based on dust modelling along the lines of sight from IR emission of five Local Group galaxies (red triangles in Fig. 11) by Leroy et al. (2011). Also, our power law index is $\sim 50\%$ higher than the one found by Arimoto et al. (1996) based on the virial masses of giant molecular clouds of the Milky Way and eight additional nearby spirals and dIs (blue dashed line). Our index, instead, is in agreement within the uncertainties with an index of ~ 1.6 derived by Genzel et al. (2012) for more massive star-forming galaxies at $z \leq 1$ assuming that galaxies follow a universal SK law of $n = 1.3$ (red line in Fig. 11). Also Schruba et al. (2012) studied the $\alpha_{\text{CO}} - Z$ relation for five HERACLES dwarf galaxies assuming a constant value for $\tau_{\text{H}_2} = 1.8$ Gyr. They found a power law index $\gtrsim 2$ (orange line in Fig. 11), significantly higher than ours.

Although the above results are qualitatively similar, quantitative differences are likely associated with the underlying assumptions behind each method, biases towards a certain galaxy class, and different dynamic ranges in metallicity, and uncertainties in its determination. In particular, the method based on a constant τ_{H_2} has the caveat that it might mask-out any true variation of the SFE with sSFR at different metallicities.

Finally, we find that in spite of the different parametrization (power-law vs. exponential) our $\alpha_{\text{CO}} - Z$ relation is broadly consistent with model predictions⁷ of Wolfire et al. (2010) from solar to $\sim 10\%$ solar metallicities.

⁷ We use models from Wolfire et al. (2010) normalized to $\alpha_{\text{CO}} = 4.4 M_\odot \text{ pc}^{-2} (\text{K km s}^{-1})^{-1}$ at solar metallicity, as presented in Sandstrom et al. (2013, see also Leroy et al. (2013)). The models assume a fixed gas mass surface density for molecular clouds and a linear scaling between the dust-to-gas ratio and metallicity.

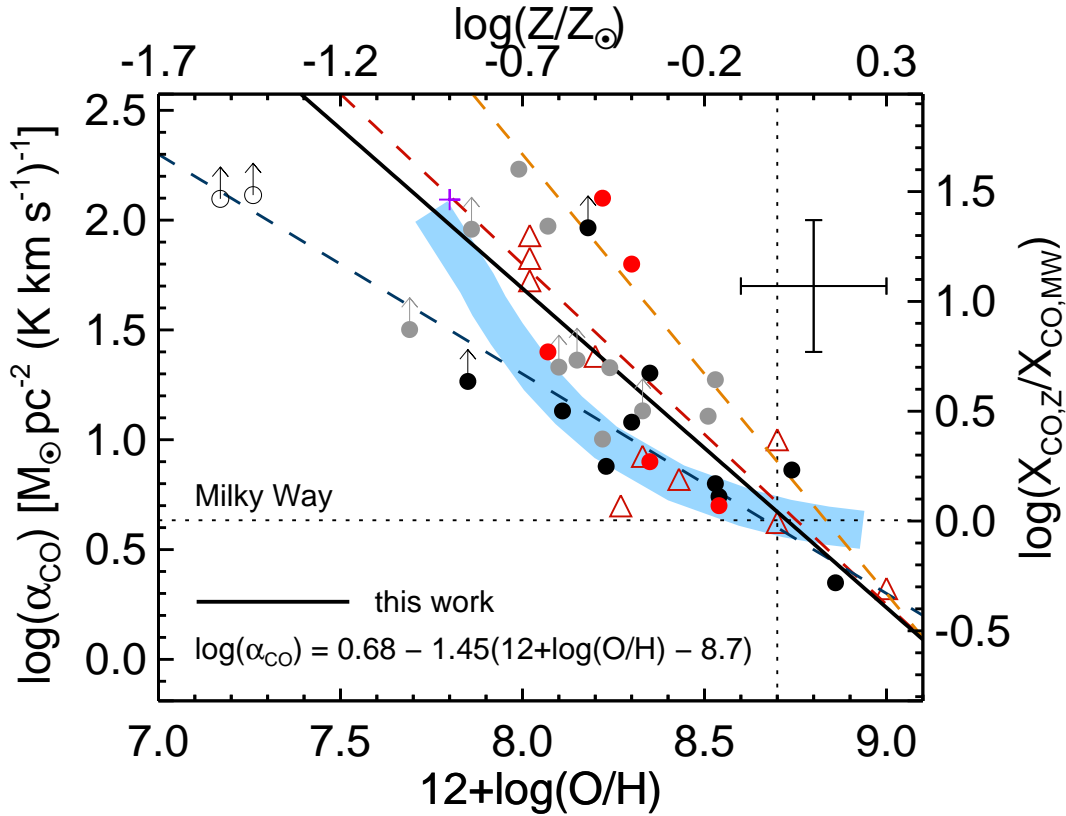


Fig. 11. CO-to-H₂ conversion factor, α_{CO} , as a function of the gas-phase metallicity. The right y-axis shows the ratio between the metallicity-dependent conversion factor and the constant value for the Milky Way (horizontal dashed line). A dotted vertical line indicates the solar metallicity. Black and grey dots show *subsample I* and *subsample II* BCDs, respectively, while the black solid line shows their best linear fit, which is indicated in the legend. Error bars indicate typical uncertainties for our sample. Red dots indicate dust-based measurements for five BCDs in our sample with *Herschel* data (see text). Triangles show dust-based measurements for Local Volume galaxies from Leroy et al. (2011), open circles are lower limits for the extremely metal-poor BCDs SBS 0335-052 and I Zw 18 (Hunt et al., 2014), and the magenta cross corresponds to the dIrr galaxy WLM from Elmegreen et al. (2013). Blue, red, and orange dashed lines show best-fits for the same relation given by Arimoto et al. (1996), Genzel et al. (2012), and Schrubba et al. (2012), respectively. The model prediction of Wolfire et al. (2010) (as presented in Sandstrom et al. (2013)) is shown as a light blue band.

7.1. Revisiting the molecular content and star formation laws

We use now the metallicity dependent CO-to-H₂ conversion factor $\alpha_{\text{CO},Z}$ obtained in the previous section in order to recompute H₂ masses and surface densities⁸. Using these quantities, we revisit different scaling relations presented before (Figs. 8–10). Thus, in Fig. 12 we show the corrected position of BCDs in the SK-law, while in Fig. 14 we show the same quantities as in Fig. 9 but using $\alpha_{\text{CO},Z}$. In Figs. 14 c–d we have included the predictions of models by Krumholz et al. (2011, magenta and blue lines, respectively).

We find that the use of a metallicity-dependent CO-to-H₂ conversion factor $\alpha_{\text{CO}}(Z)$ from Eq. 2 removes only part of the large offset position observed for BCDs in the SK law for molecular and total (H I+H₂) gas followed by more massive starbursts and late-type galaxies. In particular, our results suggest that BCDs have shorter depletion timescales compared to normal late-type disks. Starbursting dwarfs with larger gas fractions, low metallicity and higher SSFRs still show shorter depletion timescales for the molecular phase. This conclusion arises from Fig. 13 and Fig. 14 c. While some galaxies seem to agree

with Krumholz et al. (2011) models (magenta lines) predicting a constant SFE(H₂) with metallicity, some metal-poor dwarfs show a significantly increased efficiency. We note, however, that this result is in qualitative agreement with other model predictions (Pelupessy & Papadopoulos, 2009; Dib, 2011) which predict pronounced variations of τ_{H_2} with metallicity during brief periods of intense star formation. BCDs with shorter molecular depletion timescales tend to show lower molecular fractions and higher sSFR, as shown in Fig. 14 a–b and Fig. 13. The depletion timescales for molecular plus atomic gas, instead, do not appear to be a strong function of metallicity, in qualitative agreement with the models of (Krumholz et al., 2011) (blue lines).

8. Summary and conclusions

We have studied the molecular content of a large and representative sample of 21 Blue Compact Dwarf galaxies selected from a series of previous works. To this end, we have conducted new CO (1-0) and (2-1) single-dish observations of a sub-sample of 10 BCDs using the IRAM-30m telescope, further supplemented with similar data from the literature for the remaining 11 BCDs. Our CO observations have yielded 7 ($> 3\sigma$) detections, one marginal ($\sim 3\sigma$) detection in CO(2-1), and two non-detections. For two BCDs (III Zw 107 and Mrk 401) CO emis-

⁸ In order to distinguish these quantities from those derived through a Galactic CO-to-H₂ conversion factor, we have adopted a different subscript (*mol*), so M_{mol} and Σ_{mol} .

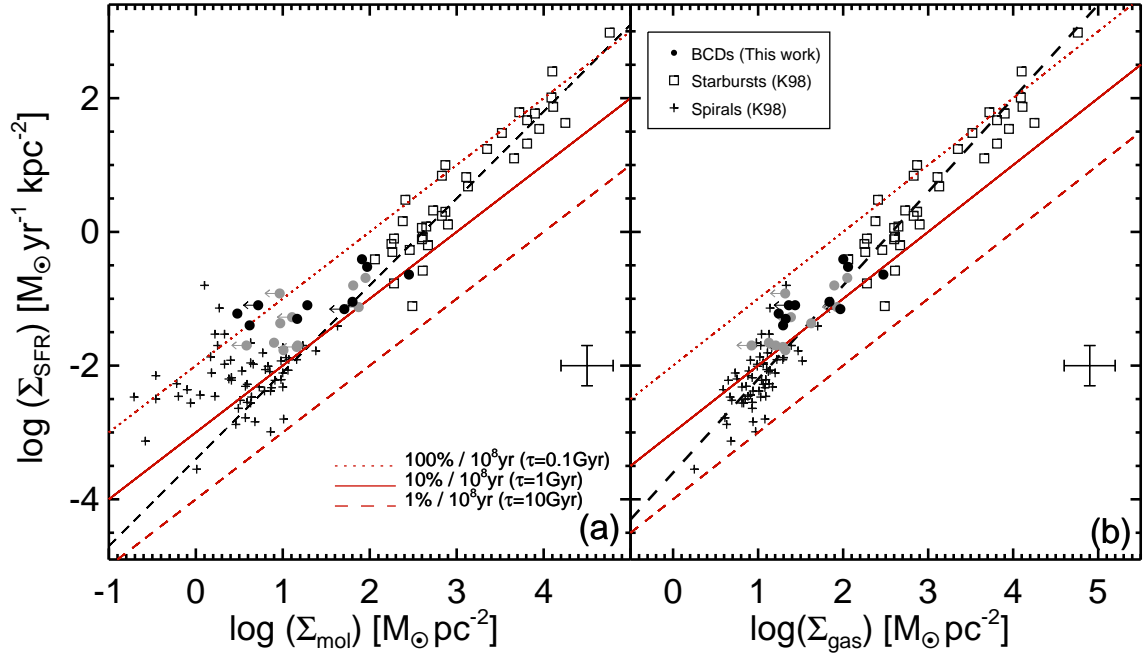


Fig. 12. Star formation rate surface density as a function of the expected H_2 (Left) and $\text{H I} + \text{H}_2$ (Right) gas surface densities after adopting the derived metallicity-dependent CO-to- H_2 conversion factor $\alpha_{\text{CO,Z}}$ from Eq. 2 (Fig. 11). Lines and symbols are as in Fig. 8.

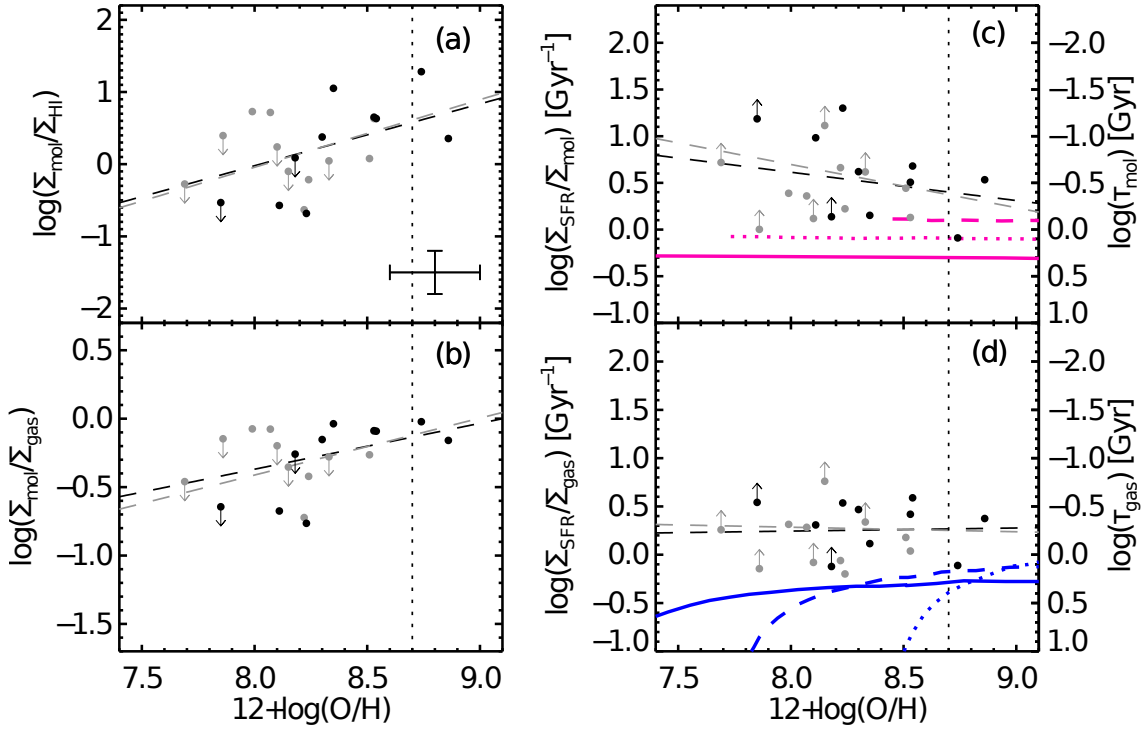


Fig. 14. Same as Fig. 9, but using the molecular masses derived using $\alpha_{\text{CO}}(Z)$ from Eq. 2 (see text). Black and grey dashed lines show linear best-fits to *subsample I* and *subsample II*. Solid, dotted and dashed magenta (blue) lines in panel *c* (*d*) show model predictions by Krumholz et al. (2011) for different values of Σ_{gas} (80, 20 and 5 $\text{M}_\odot \text{pc}^{-2}$, respectively).

sion has been detected for the first time. The derived CO luminosities, in combination with an extensive ancillary data set, have been used to study their relation to several galaxy-averaged properties, including SFR tracers, stellar and H I masses, sizes and metallicity, as well as their impact on the star formation laws. We summarize our conclusions in the following:

- The amount of molecular mass traced by CO in BCDs scales with both stellar and H I gas masses and all SFR tracers studied so far, in good agreement with previous findings for dwarf galaxies in general. Our results suggest that, over galaxy-wide scales, more massive and luminous BCDs – which are those with strong and extended star-forming re-

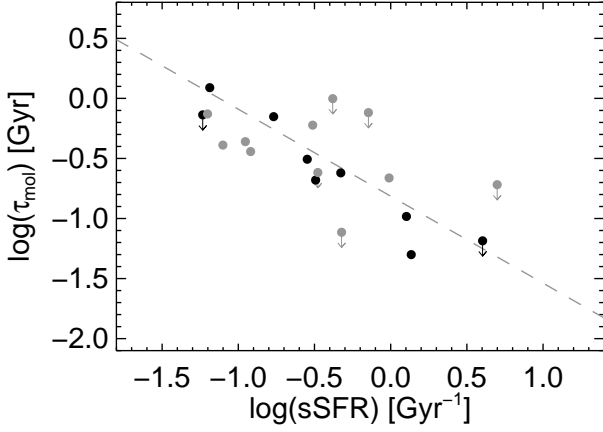


Fig. 13. Molecular depletion timescale, as derived using $\alpha_{\text{CO},Z}$ from Eq. 2 (see text), as a function of the *specific* SFR. Symbols and line are as in Fig. 10b.

gions – are favoured for CO detections. However, CO luminosity is a strong function of the gas-phase metallicity, which puts the most stringent constraint ($Z \gtrsim 0.3 Z_{\odot}$) to the CO detectability in BCDs.

- In the context of the Schmidt-Kennicutt law, BCDs show larger SFR surface densities compared with other late-type galaxies. Thus, they appear systematically offset to lower H_2 and H_2+HI depletion timescales from the general trend followed by dwarfs irregulars, spiral discs and more massive and dusty starbursts. We find a strong correlation between the BCD metallicity and both the molecular gas fraction and the molecular gas depletion timescale; more metal-poor BCDs show lower molecular gas fractions and shorter depletion timescales than more metal-rich BCDs. However, for the *total* (molecular plus atomic) gas depletion timescale the metallicity dependence becomes significantly reduced. Overall, we find that more metal-poor, gas-rich, and high sSFR BCDs are those with shorter H_2 depletion timescales, under the assumption of a constant (Milky Way) CO-to- H_2 conversion factor.
- We discuss the above results in the context of the CO-to- H_2 conversion factor α_{CO} . We have derived a metallicity-dependent CO-to- H_2 conversion factor using the relation between τ_{H_2} and metallicity, under the assumption that the empirical correlation between the specific SFR and τ_{H_2} , found more metal-rich galaxies in the COLDMASS survey (Saintonge et al., 2011) can be extended to lower masses. The result is $\log(\alpha_{\text{CO},Z}) = 0.7 - 1.5 \times (12 + \log(O/H) - 8.7)$ (or $\alpha_{\text{CO},Z} \propto (Z/Z_{\odot})^{-y}$, with $y = 1.5 \pm 0.3$). This power law is in qualitative agreement with previous determinations based on dust-based H_2 masses and the model predictions of Wolfire et al. (2010). Our power law index is however higher than values based on virial masses of molecular clouds, and slightly lower than values found assuming an universal τ_{H_2} (e.g., Schrubba et al., 2012; Genzel et al., 2012). This result suggest that in vigorously star-forming dwarfs the fraction of H_2 traced by CO decreases a factor of about 40 from $Z \sim Z_{\odot}$ to $Z \sim 0.1 Z_{\odot}$, leading to a strong underestimation of the H_2 mass in metal-poor systems when a Galactic $X_{\text{CO},\text{MW}}$ is considered. This supports previous work suggesting that in metal-poor and highly ionized environments –such as those in high sSFR BCDs– massive star formation is found in increasingly CO-free molecular clouds. According to models (e.g., Wolfire et al., 2010) this is likely due to a rapid de-

crease of dust shielding and, consequently, strong UV photodissociation (see also Bolatto et al., 2013).

- The observed relations between H_2 , SFR and metallicity change when adopting the metallicity-dependent α_{CO} , alleviating the offset position of BCDs in the SK laws but not removing it completely. Our analysis suggest that *starbursting dwarfs have shorter depletion gas timescales compared to normal late-type discs even accounting for the molecular gas not traced by CO emission in metal-poor environments*. Thus, τ_{mol} appears not constant with metallicity but showing a small increase with metallicity mainly driven by galaxies with higher sSFR and gas fraction. While this produces some tension with some models (Krumholz et al., 2011) it appears to agree qualitatively with model predictions for brief and intense episodes of star formation (Pelupessy & Papadopoulos, 2009; Dib et al., 2011). While the revised relations between the molecular to atomic gas surface density ratio and molecular fraction with metallicity show a shallower slope, the total (H_2+HI) gas depletion timescale tend to become nearly constant with metallicity, in qualitative agreement with model predictions by Krumholz et al. (2011).

We note that in the process of refereeing of the present paper a work by Hunt et al. (2015) tackling similar goals has just appeared published. Their results on the CO emission of 8 low-metallicity dwarf galaxies are certainly complementary to the work presented here, and their conclusions on the molecular depletion timescales of such galaxies appear in good agreement with ours.

Further insights on the above conclusions would benefit from future studies using larger samples of star-forming dwarfs for which large and homogeneous multiwavelength datasets are currently available (e.g., the AVOCADO project, Sánchez-Janssen et al., 2013).

Being rare in the Local Universe, BCDs are one of the best local analogues of low-mass star-forming galaxies at high redshift. The strong limitations found on the use of CO as a suitable tracer of the molecular gas involved in the onset of starburst activity in nearby BCDs clearly underline the strong challenge that will constitute to trace the molecular content of chemically unevolved galaxies in the early Universe, even using the unprecedented sensitivity of ALMA.

Acknowledgements. The authors would like to thank the referee, J. Braine, for his helpful reports which significantly contributed to improving this manuscript. We are grateful to the staff of the IRAM 30m telescope for their support during the observations, and in particular to Sergio Martín. We thank U. Lisenfeld, J.M. Vílchez, P. Papaderos and S. Dib for helpful comments on the analysis. A significant part of this work has been presented in the PhD Thesis of R. A. (Universidad de La Laguna, Spain, October 2008). This work has been partially funded by the Spanish DGCyT, grants AYA2010-21887-C04-01, AYA2010-21887-C04-04, AYA2013-47742-C4-2-P, AYA2012-32295, AYA2013-43188-P, and FIS2012-32096. This research was partially funded by the Spanish MEC under the Consolider-Ingenio 2010 Program grant CSD2006-00070: First Science with the GTC (<http://www.iac.es/consolider-ingenio-gtc/>). R. A. also acknowledges the contribution of the FP7 SPACE project ASTRODEEP (Ref.No: 312725), supported by the European Commission.

This research has made use of the NASA/IPAC Extragalactic Database (NED) which is operated by the Jet Propulsion Laboratory, California Institute of Technology, under contract with the National Aeronautics and Space Administration.

References

- Albrecht, M., Chini, R., Krügel, E., Müller, S. A. H., & Lemke, R. 2004, A&A, 414, 141
- Allende Prieto, C., Lambert, D. L., & Asplund, M. 2001, ApJ, 556, L63

- Amorín, R. O., Muñoz-Tuñón, C., Aguerri, J. A. L., Cairós, L. M., & Caon, N. 2007, *A&A*, 467, 541
- Amorín, R., PhD Thesis, 2008, Universidad de La Laguna, Spain. ISBN: 978-84-692-1603-3
- Amorín, R., Aguerri, J. A. L., Muñoz-Tuñón, C., & Cairós, L. M. 2009, *A&A*, 501, 75
- Amorín, R. O., Pérez-Montero, E., & Vílchez, J. M. 2010, *ApJ*, 715, L128
- Amorín, R. O. 2010, *PASP*, 122, 495
- Amorín, R., Pérez-Montero, E., Vílchez, J. M., & Papaderos, P. 2012, *ApJ*, 749, 185
- Amorín, R., Sommariva, V., Castellano, M., et al. 2014, *A&A*, 568, L8
- Amorín, R., Grazian, A., Castellano, M., et al. 2014, *ApJ*, 788, L4
- Amorín, R., Pérez-Montero, E., Contini, T., et al. 2015, *A&A*, 578, A105
- Arimoto, N., Sofue, Y., & Tsujimoto, T. 1996, *PASJ*, 48, 275
- Barone, L. T., Heithausen, A., Hüttemeister, S., Fritz, T., & Klein, U. 2000, *MNRAS*, 317, 649
- Bekki, K. 2008, *MNRAS*, 388, L10
- Bell, E. F., & de Jong, R. S. 2001, *ApJ*, 550, 212
- Bigiel, F., Leroy, A., Walter, F., Brinks, E., de Blok, W. J. G., Madore, B., & Thornley, M. D. 2008, *AJ*, 136, 2846
- Bigiel, F., Leroy, A. K., Walter, F., et al. 2011, *ApJ*, 730, L13
- Bolatto, A. D., Leroy, A. K., Jameson, K., et al. 2011, *ApJ*, 741, 12
- Bolatto, A. D., Wolfire, M., & Leroy, A. K. 2013, *ARA&A*, 51, 207
- Boselli, A., Cortese, L., Boquien, M., et al. 2014, *A&A*, 564, A66
- Brinchmann, J., Charlot, S., White, S. D. M., et al. 2004, *MNRAS*, 351, 1151
- Brosch, N., Almozino, E., & Heller, A. B. 2004, *MNRAS*, 349, 357
- Buat, V., et al. 2005, *ApJ*, 619, L51
- Buisson, G., Desbats, L., Duvert, G., et al. 1997, *Continuum and Line Analysis Single-dish Software*, Observatoire de Grenoble and IRAM
- Campos-Aguilar, A., Moles, M., & Masegosa, J. 1993, *AJ*, 106, 1784
- Cairós, L. M., Vílchez, J. M., González Pérez, J. N., Iglesias-Páramo, J., & Caon, N. 2001, *ApJS*, 133, 321
- Cairós, L. M., Caon, N., Vílchez, J. M., González-Pérez, J. N., & Muñoz-Tuñón, C. 2001, *ApJS*, 136, 393
- Cairós, L. M., Caon, N., Papaderos, P., Noeske, K., García-Lorenzo, B., Vílchez, J., & Muñoz-Tuñón, C. 2003, *ApJ*, 593, 312
- Cairós, L. M., Caon, N., García-Lorenzo, B., Monreal-Ibero, A., Amorín, R., Weilbacher, P., & Papaderos, P. 2007, *ApJ*, 669, 251
- Caon, N., Cairós, L. M., Aguerri, J. A. L., & Muñoz-Tuñón, C. 2005, *ApJS*, 157, 218
- Cardelli, J. A., Clayton, G. C., & Mathis, J. S. 1989, *ApJ*, 345, 245
- Condon, J. J., Cotton, W. D., Greisen, E. W., Yin, Q. F., Perley, R. A., Taylor, G. B., & Broderick, J. J. 1998, *AJ*, 115, 1693
- Cormier, D., Madden, S. C., Lebouteiller, V., et al. 2014, *A&A*, 564, A121
- Dame, T. M., Hartmann, D., & Thaddeus, P. 2001, *ApJ*, 547, 792
- Dale, D. A., Helou, G., Neugebauer, G., et al. 2001, *AJ*, 122, 1736
- Dale, D. A., & Helou, G. 2002, *ApJ*, 576, 159
- Davies, J. I., & Philipps, S. 1988, *MNRAS*, 233, 553
- de Barros, S., Vanzella, E., Amorín, R., et al. 2015, *arXiv:1507.06648*
- Dib, S. 2011, *ApJ*, 737, L20
- Dib, S., Piau, L., Mohanty, S., & Braine, J. 2011, *MNRAS*, 415, 3439
- Draine, B. T., Dale, D. A., Bendo, G., et al. 2007, *ApJ*, 663, 866
- Elfagh, T., Booth, R. S., Hoeglund, B., Johansson, L. E. B., & Sandqvist, A. 1996, *A&AS*, 115, 439
- Elmegreen, B. G., Zhang, H.-X., & Hunter, D. A. 2012, *ApJ*, 747, 105
- Elmegreen, B. G., Rubio, M., Hunter, D. A., et al. 2013, *Nature*, 495, 487
- Ekta, B., & Chengalur, J. N. 2010, *MNRAS*, 403, 295
- Filho, M. E., Winkel, B., Sánchez Almeida, J., et al. 2013, *A&A*, 558, A18
- Frayser, D. T., Seaquist, E. R., Thuan, T. X., & Sievers, A. 1998, *ApJ*, 503, 231
- Fumagalli, M., Krumholz, M. R., & Hunt, L. K. 2010, *ApJ*, 722, 919
- García-Lorenzo, B., Cairós, L. M., Caon, N., Monreal-Ibero, A., & Kehrig, C. 2008, *ApJ*, 677, 201
- Gardan, E., Braine, J., Schuster, K. F., Brouillet, N., & Sievers, A. 2007, *A&A*, 473, 91
- Garland, C. A., Williams, J. P., Pisano, D. J., et al. 2005, *ApJ*, 624, 714
- Genzel, R., Tacconi, L. J., Combes, F., et al. 2012, *ApJ*, 746, 69
- Gerola, H., Seiden, P. E., & Schulman, L. S. 1980, *ApJ*, 242, 517
- Gil de Paz, A., Madore, B. F., & Pevunova, O. 2003, *ApJS*, 147, 29
- Gil de Paz, A., & Madore, B. F. 2005, *ApJS*, 156, 345
- Glover, S. C. O., & Mac Low, M.-M. 2011, *MNRAS*, 412, 337
- Glover, S. C. O., & Clark, P. C. 2012, *MNRAS*, 426, 377
- Gnedin, N. Y., & Kravtsov, A. V. 2010, *ApJ*, 714, 287
- Gordon, D., & Gottesman, S. T. 1981, *AJ*, 86, 161
- Gratier, P., Braine, J., Rodríguez-Fernández, N. J., et al. 2010a, *A&A*, 522, A3
- Gratier, P., Braine, J., Rodríguez-Fernández, N. J., et al. 2010b, *A&A*, 512, A68
- Helou, G., Khan, I. R., Malek, L., & Boehmer, L. 1988, *ApJS*, 68, 151
- Hollenbach, D. J., & Tielens, A. G. G. M. 1999, *Reviews of Modern Physics*, 71, 173
- Huang, M.-L., & Kauffmann, G. 2014, *MNRAS*, 443, 1329
- Hunt, L., Magrini, L., Galli, D., et al. 2012, *MNRAS*, 427, 906
- Hunt, L. K., Testi, L., Casasola, V., et al. 2014, *A&A*, 561, AA49
- Hunt, L. K., García-Burillo, S., Casasola, V., et al. 2015, *A&A*, 583, A114
- Hunter, D. A., & Elmegreen, B. G. 2004, *AJ*, 128, 2170
- Hunter, D. A., & Elmegreen, B. G. 2006, *ApJS*, 162, 49
- Israel, F. P. 1997, *A&A*, 328, 471
- Israel, F. P. 2005, *A&A*, 438, 855
- Izotov, Y. I., Papaderos, P., Guseva, N. G., Fricke, K. J., & Thuan, T. X. 2006, *A&A*, 454, 137
- Jarrett, T. H., Chester, T., Cutri, R., Schneider, S., Skrutskie, M., & Huchra, J. P. 2000, *AJ*, 119, 2498
- Kennicutt, R. C., Jr. 1998, *ApJ*, 498, 541
- Kennicutt, R. C., et al. 2009, *ApJ*, 703, 1672
- Kennicutt, R. C., & Evans, N. J. 2012, *ARA&A*, 50, 531
- Kniazev, A. Y., Pustilnik, S. A., Grebel, E. K., Lee, H., & Pramskij, A. G. 2004, *ApJS*, 153, 429
- Koulouridis, E., Plionis, M., Chávez, R., et al. 2013, *A&A*, 554, AA13
- Krumholz, M. R., McKee, C. F., & Tumlinson, J. 2009, *ApJ*, 699, 850
- Krumholz, M. R., Leroy, A. K., & McKee, C. F. 2011, *ApJ*, 731, 25
- Kunth, D., Östlin, G. 2000, *A&A Rev.*, 10, 1
- Lagos, P., Telles, E., & Melnick, J. 2007, *A&A*, 476, 89
- Lee, J. C., Gil de Paz, A., Kennicutt, R. C., Jr., et al. 2011, *ApJS*, 192, 6
- Leon, S., Combes, F., & Menon, T. K. 1998, *A&A*, 330, 37
- Lelli, F., Fraternali, F., & Verheijen, M. 2014, *A&A*, 563, A27
- Lelli, F., Verheijen, M., & Fraternali, F. 2014, *A&A*, 566, A71
- Leroy, A., Bolatto, A. D., Simon, J. D., & Blitz, L. 2005, *ApJ*, 625, 763
- Leroy, A., Bolatto, A., Walter, F., & Blitz, L. 2006, *ApJ*, 643, 825
- Leroy, A., Cannon, J., Walter, F., Bolatto, A., & Weiss, A. 2007, *ApJ*, 663, 990
- Leroy, A. K., Walter, F., Brinks, E., Bigiel, F., de Blok, W. J. G., Madore, B., & Thornley, M. D. 2008, *AJ*, 136, 2782
- Leroy, A. K., Bolatto, A., Gordon, K., et al. 2011, *ApJ*, 737, 12
- Leroy, A. K., Walter, F., Sandstrom, K., et al. 2013, *AJ*, 146, 19
- López-Sánchez, Á. R., & Esteban, C. 2010, *A&A*, 517, A85
- López-Sánchez, Á. R., Koribalski, B. S., van Eymeren, J., et al. 2012, *MNRAS*, 419, 1051
- Mac Low, M.-M., & Ferrara, A. 1999, *ApJ*, 513, 142
- Madden, S. C., Poglitsch, A., Geis, N., Stacey, G. J., & Townes, C. H. 1997, *ApJ*, 483, 200
- Martin, D. C., et al. 2005, *ApJ*, 619, L1
- Martín-Manjón, M. L., Mollá, M., Díaz, A. I., & Terlevich, R. 2012, *MNRAS*, 420, 1294
- Maseda, M. V., van der Wel, A., Rix, H.-W., et al. 2014, *ApJ*, 791, 17
- McQuinn, K. B. W., Skillman, E. D., Dalcanton, J. J., et al. 2012, *ApJ*, 751, 127
- Micheva, G., Östlin, G., Bergvall, N., et al. 2013, *MNRAS*, 431, 102
- Morales-Luis, A. B., Sánchez Almeida, J., Aguerri, J. A. L., & Muñoz-Tuñón, C. 2011, *ApJ*, 743, 77
- Morrissey, P., et al. 2005, *ApJ*, 619, L7
- Moshir, M., & et al. 1990, *IRAS Faint Source Catalogue*, version 2.0 (1990), 0
- Moustakas, J., & Kennicutt, R. C., Jr. 2006, *ApJ*, 651, 155
- Narayanan, D., Krumholz, M. R., Ostriker, E. C., & Hernquist, L. 2012, *MNRAS*, 421, 3127
- Noeske, K. G., Iglesias-Páramo, J., Vílchez, J. M., Papaderos, P., & Fricke, K. J. 2001, *A&A*, 371, 806
- Noeske, K. G., Papaderos, P., Cairós, L. M., & Fricke, K. J. 2003, *A&A*, 410, 481
- Noeske, K. G., Papaderos, P., Cairós, L. M., & Fricke, K. J. 2005, *A&A*, 429, 115
- Noeske, K. G., Weiner, B. J., Faber, S. M., et al. 2007, *ApJ*, 660, L43
- Papaderos, P., Loose, H.-H., Thuan, T. X., & Fricke, K. J. 1996a, *A&AS*, 120, 207
- Papaderos, P., Loose, H.-H., Fricke, K. J., & Thuan, T. X. 1996b, *A&A*, 314, 59
- Papaderos, P., Guseva, N. G., Izotov, Y. I., Noeske, K. G., Thuan, T. X., & Fricke, K. J. 2006, *A&A*, 457, 45
- Papaderos, P., Guseva, N. G., Izotov, Y. I., & Fricke, K. J. 2008, *A&A*, 491, 113
- Pelupessy, F. I., & Papadopoulos, P. P. 2009, *ApJ*, 707, 954
- Pérez-Montero, E., & Díaz, A. I. 2003, *MNRAS*, 346, 105
- Pérez-Montero, E., & Contini, T. 2009, *MNRAS*, 398, 949
- Press, W. H., Teukolsky, S. A., Vetterling, W. T., & Flannery, B. P. 1992, *Cambridge: University Press*, —1992, 2nd ed.,
- Pustilnik, S. A., Kniazev, A. Y., Lipovetsky, V. A., & Ugryumov, A. V. 2001, *A&A*, 373, 24
- Recchi, S., & Hensler, G. 2013, *A&A*, 551, A41
- Rémy-Ruyer, A., Madden, S. C., Galliano, F., et al. 2014, *A&A*, 563, A31
- Rémy-Ruyer, A., Madden, S. C., Galliano, F., et al. 2015, *A&A*, 582, A121
- Rubio, M., Lequeux, J., & Boulanger, F. 1993, *A&A*, 271, 9
- Rubio, M., Elmegreen, B. G., Hunter, D. A., et al. 2015, *Nature*, 525, 218
- Saintonge, A., Kauffmann, G., Wang, J., et al. 2011b, *MNRAS*, 415, 61

- Saintonge, A., Kauffmann, G., Kramer, C., et al. 2011a, MNRAS, 415, 32
- Sánchez Almeida, J., Muñoz-Tuñón, C., Amorín, R., et al. 2008, ApJ, 685, 194
- Sánchez Almeida, J., Muñoz-Tuñón, C., Elmegreen, D. M., Elmegreen, B. G., & Méndez-Abreu, J. 2013, ApJ, 767, 74
- Sánchez Almeida, J., Morales-Luis, A. B., Muñoz-Tuñón, C., et al. 2014, ApJ, 783, 45
- Sánchez Almeida, J., Elmegreen, B. G., Muñoz-Tuñón, C., et al. 2015, ApJ, 810, L15
- Sánchez-Janssen, R., Amorín, R., García-Vargas, M., et al. 2013, A&A, 554, A20
- Sandstrom, K. M., Leroy, A. K., Walter, F., et al. 2013, ApJ, 777, 5
- Sargent, W. L. W., & Searle, L. 1970, ApJ, 162, L155
- Shi, F., Kong, X., & Cheng, F. Z. 2006, A&A, 453, 487
- Shi, Y., Helou, G., Yan, L., et al. 2011, ApJ, 733, 87
- Shi, Y., Wang, J., Zhang, Z.-Y., et al. 2015, ApJ, 804, L11
- Schlegel, D. J., Finkbeiner, D. P., & Davis, M. 1998, ApJ, 500, 525
- Schmidt, M. 1959, ApJ, 129, 243
- Schruba, A., Leroy, A. K., Walter, F., et al. 2011, AJ, 142, 37
- Schruba, A., Leroy, A. K., Walter, F., et al. 2012, AJ, 143, 138
- Silich, S., & Tenorio-Tagle, G. 2001, ApJ, 552, 91
- Solomon, P. M., Downes, D., Radford, S. J. E., & Barrett, J. W. 1997, ApJ, 478, 144
- Strong, A. W., & Mattox, J. R. 1996, A&A, 308, L21
- Taylor, C. L., Kobulnicky, H. A., & Skillman, E. D. 1998, AJ, 116, 2746
- Tacconi, L. J., & Young, J. S. 1987, ApJ, 322, 681
- Telles, E., & Terlevich, R. 1995, MNRAS, 275, 1
- Tenorio-Tagle, G., Muñoz-Tuñón, C., Pérez, E., Silich, S., & Telles, E. 2006, ApJ, 643, 186
- Terlevich, R., Melnick, J., Masegosa, J., Moles, M., & Copetti, M. V. F. 1991, A&AS, 91, 285
- Thuan, T. X., & Martin, G. E. 1981, ApJ, 247, 823
- Vaduvescu, O., Richer, M. G., & McCall, M. L. 2006, AJ, 131, 1318
- van Zee, L., Skillman, E. D., & Salzer, J. J. 1998, AJ, 116, 1186
- van Zee, L., Salzer, J. J., & Skillman, E. D. 2001, AJ, 122, 121
- Verdes-Montenegro, L., Yun, M. S., Perea, J., del Olmo, A., & Ho, P. T. P. 1998, ApJ, 497, 89
- Vílchez, J. M., & Iglesias-Páramo, J. 1998, ApJ, 508, 248
- Wei, L. H., Vogel, S. N., Kannappan, S. J., et al. 2010, ApJ, 725, L62
- Wilson, C. D. 1995, ApJ, 448, L97
- Wolfire, M. G., Hollenbach, D., & McKee, C. F. 2010, ApJ, 716, 1191
- Zhao, Y., Gao, Y., & Gu, Q. 2010, ApJ, 710, 663
- Zhao, Y., Gao, Y., & Gu, Q. 2013, ApJ, 764, 44